

Observational Predictions of LQG Motivated Polymerized Black Holes and Constraints From Sgr A* and M87*

Rahul Kumar Walia^{a*}

^a *Astrophysics Research Centre, School of Mathematics, Statistics and Computer Science,
University of KwaZulu-Natal, Private Bag 54001, Durban 4000, South Africa*

(Dated: July 6, 2022)

Loop Quantum Gravity (LQG) inspired partial polymer quantization in four-dimensional theory leads to a single-horizon quantum corrected globally regular black hole spacetime. The polymerized black hole metric is characterized by the minimum length parameter, k , and mimics the Schwarzschild black hole in the weak-field limit. We present an analytic and numerical investigation of the strong gravitational lensing and shadow morphology to determine the observational impacts of quantum effects. We calculate the characteristic changes in the lensing observables compared to those for the Schwarzschild black hole. It is interesting to note that the deflection angle, the angular separation between the outermost relativistic image, and magnification increase with k . Using the ray-tracing technique, we simulated the black hole shadows under three distinct optically thin accretion models: static spherical accretion, radially infalling spherical accretion, and the thin accretion disk model. Polymerized black holes' shadow morphology strongly depends on k . Constraints on k are derived for the M87* and Sgr A* black hole shadow observations from the Event Horizon Telescope. Our study suggests that quantum gravity effects are accessible in the astrophysical black holes' observations.

I. INTRODUCTION

The presence of spacetime singularities, manifested as curvature scalar divergence or geodesic incompleteness, is an undesirable but apparently inevitable feature of general relativity and many other alternate classical theories of gravity [1, 2]. Several independent attempts through quantum gravity models have been made to evade the ultra-violet incompleteness of general relativity and to regularize the curvature invariant. In this direction, Loop Quantum Gravity (LQG) turned out to be one of the few successful attempts to understand the quantum nature of gravity [3]. LQG is one of the non-perturbative and background-independent approaches to quantum gravity. It has been shown that the underlying idea of quantization of area and volume observables is the fundamental ingredient in the LQG models to solve the black hole singularity problem [4–7]. In particular, the S^2 sphere bounces on the non-zero minimum area of LQG black hole models, and the central curvature singularity disappears. However, because of the inherent complexity involved in the complete quantum treatment of LQG, it is easier to work with an effective-field theory approach. In this line of research, the phase space quantization or semi-classical polymerization that preserves the LQG's idea of spacetime discreteness turns out to be very interesting and fruitful [8, 9]. Peltola and Kunstatler [10, 11] have reported that polymerization of the generalized area variable alone leads to a complete, regular, single-horizon spacetime, in which the classical singularity is replaced by a bounce. This four-dimensional quantum-corrected polymerized black hole

spacetime has fascinating properties and advantages over other regular black hole candidates, including: (i) single horizon, which eliminates the problem of mass inflation at the inner horizon, (ii) globally hyperbolic spacetime, (iii) the global spacetime structure is quite different from other regular black holes, in that the areal radius decreases to a minimum value in the black hole interior and then re-expands into a Kantowski-Sachs universe (iv) geodesically complete spacetime. Interestingly, Daghighi *et al.* [12] have proven that these black holes are stable against small massless scalar perturbations, contrary to other regular black holes [13]. Bronnikov *et al.* [14] called the black bounce black hole with single horizon as the “black universe”.

The possible observational signatures of the quantum nature of gravity are largely unexplored for astrophysical systems. One can therefore ask whether the resulting LQG-motivated corrections around $r = 0$ can propagate to the black hole exterior and leave imprints on the black hole's observational features. To put it another way, is it possible to use the black hole observational features, particularly in the electromagnetic spectrum, to extract information about the quantum gravity signatures in the black hole spacetime. We address these questions in this paper? We investigate the gravitational lensing of light around the polymerized black hole, and calculate the direct and relativistic image positions, magnification, and time delay in the formation of primary and secondary images. We compute the effects of the polymer parameter on the lensing observables and compare them with those for the Schwarzschild black hole. One of the salient features of strong gravitational lensing by a black hole is the logarithmic divergence of the deflection angle in the impact parameter [15, 16]. This divergence accounts for the formation of a photon sphere around the black hole and the existence of a

* KumarR@ukzn.ac.za

photon ring enclosing the “black hole shadow” [17]. Following that, we construct the polymerized black hole shadows under various accretion flow models to get a better insight into the causal and observational features of emission arising near a polymerized black hole. While the photon ring solely depends on the spacetime metric, in astrophysically realistic scenarios, the optical appearance of a black hole is highly dependent on the details of the accretion models and the emission process. Consequently, by comparing the intensity distribution in synthetic shadows, one can assess the differences/similarities between the polymerized and Schwarzschild black hole shadows. In a magnificent achievement, EHT made the first horizon-scale radio observations of the supermassive black holes Sgr A* and M87* and unraveled their characteristic shadows enclosed with a bright photon emission ring [18–24]. We constrain the polymer parameter using the EHT shadow results. Therefore, the present study is not only crucial to discovering the impact of quantum gravity corrections on the observational aspects of the black hole, it is also relevant in light of the EHT observations. Gravitational lensing and shadows of other classes of quantum gravity black holes have also been investigated [25–32].

The study of gravitational lensing was led by Einstein [33] and Darwin [34] in the weak-field limit, and later the theory was developed systematically in the strong-field limits as well [35–40]. However, Virbhadra [41–43], Bozza et al. [15, 16, 44–46], and Tsukamoto [47–50] brought a significant interest into the field and provided an analytical framework to investigate the strong gravitational lensing effect for a generic static spherically symmetric metric. A black hole’s shadow is a manifestation of the strong gravitational lensing around it. Black holes embedded in the optically thin accreting region are expected to reveal a dark “shadow” caused by the photon capture and strong gravitational lensing [17, 51]. Luminet [52] presented a visual appearance of a thin emitting accretion disk around the Schwarzschild black hole. Similar hot accretion flows are found around many supermassive black holes in the universe, and they are natural candidates to reveal shadows in their images [53]. The black hole shadow theory has evolved over the past decades and has resulted in a flourish of studies (see [54, 55] for review). Lately, the strong gravitational lensing [56–67] and black hole shadow [31, 68–95] have been extensively used in testing theories of gravity at the horizon-scale regime, black hole parameter estimation, and deducing the nature of any matter distributions in the black hole background. Therefore, strong gravitational lensing features and shadows can be used as an effective way to study polymerized black holes and can provide us with valuable information about the underlying quantum gravitational corrections.

The rest of the paper is organized as follows. In Sect. II, we discuss the geometric properties of the static spherically symmetric polymerized black hole and demonstrate that this metric appears as an exact solution

of the Einstein field equations minimally coupled with the phantom scalar field and the nonlinear electrodynamics field (NED) associated with the magnetic field. In Sect. III, we present the study of gravitational lensing in the weak and strong deflection limits. The image positions, magnifications, Einstein ring, strong-lensing observables, and numerical estimations of deflection angle are presented in Sect. IV. In Sect. V, lensing by supermassive black holes Sgr A* and M87* is discussed. The polymerized black hole shadows under different accretion flow models are reported in Sect. VI, and constraints on the polymer parameter are deduced using the Sgr A* and M87* black hole shadow observational data in Sect. VIII. Finally, we summarize our main findings in Sect. VIII.

II. LQG MOTIVATED 4D POLYMERIZED BLACK HOLE

The dynamical field equations in the four-dimensional partially polymerized theory admit a static and spherically symmetric black hole solution [10, 11]

$$ds^2 = -A(r)dt^2 + B(r)dr^2 + C(r)(d\theta^2 + \sin^2\theta d\phi^2), \quad (1)$$

with

$$A(r) = \left(\sqrt{1 - \frac{k^2}{r^2}} - \frac{2M}{r} \right),$$

$$B(r) = \left(\left(\sqrt{1 - \frac{k^2}{r^2}} - \frac{2M}{r} \right) \left(1 - \frac{k^2}{r^2} \right) \right)^{-1}, \quad C(r) = r^2.$$

The black hole metric depends on two parameters: black hole mass M and polymer parameter k . The solution is asymptotically flat at $r \rightarrow \infty$, and the Ricci and Kretschmann scalars are everywhere finite, and vanish rapidly at far distances from the black hole. As a result, the polymerized black hole metric describes a globally regular spacetime. One of the most striking features of this four-dimensional quantum-corrected black hole metric (1) is that it has a single horizon at $r \equiv r_+ = \sqrt{4M^2 + k^2}$. From the metric function, it is clear that $r \geq k$; the radial coordinate r admits a minimum value at $r = k$ in a nonstatic ($A(r) < 0$) spacetime region and called as “black bounce”. Notably, the curvature singularity at $r = 0$ is now replaced by a sphere of radius $r = k$ bouncing into an infinitely expanding Kantowski-Sachs spacetime. The parameter k defines the minimum radius of the bounce, such that for $k \rightarrow 0$ metric (1) recovers the Schwarzschild black hole metric. It immediately follows that the energy conditions are violated at the center. Bronnikov *et al.* [14, 96–98] have shown that geometries containing a black bounce are described by solutions to the Einstein equations with phantom scalar fields. Nevertheless, the coordinate singularity at $r = k$, can be transformed away by

using the transformation $r = \sqrt{k^2 + y^2}$; the transformed metric reads as

$$ds^2 = - \left(\frac{y - 2M}{\sqrt{y^2 + k^2}} \right) dt^2 + \frac{1}{\left(\frac{y - 2M}{\sqrt{y^2 + k^2}} \right)} dy^2 + (y^2 + k^2)(d\theta^2 + \sin^2 \theta d\phi^2). \quad (2)$$

Here, the radial coordinate y assume the full range $0 \leq y \leq \infty$. Most of the regular black holes that are closely connected to a potential theory of quantum gravity, can not be viewed as derived from, but rather *inspired* by quantum gravity. As such, they constitute useful phenomenological models but making their physical justification less straightforward [99]. Here, we present the source for this polymerized black hole. Considering the validity of the Einstein field equations $G_{\mu\nu} = T_{\mu\nu}$ (with $8\pi G = 1$), we calculate the corresponding energy-momentum tensor (EMT) for the metric (2):

$$T_t^t \equiv G_t^t = \frac{-(k^2 + y^2)^{3/2} + y^3 - k^2(4M - 3y)}{(k^2 + y^2)^{5/2}}, \quad (3)$$

$$T_r^r \equiv G_r^r = \frac{y}{(k^2 + y^2)^{3/2}} - \frac{1}{k^2 + y^2}, \quad (4)$$

$$T_\theta^\theta \equiv G_\theta^\theta = \frac{k^2(y - 2M)}{2(k^2 + y^2)^{5/2}}. \quad (5)$$

We start with the Einstein-Hilbert action and a minimally coupled uncharged scalar field $\Phi(x)$ and the NED field with Lagrangian density $\mathcal{L}(\mathcal{F})$ [100]

$$S = \int \sqrt{-g} d^4x (\mathcal{R} + 2\epsilon g^{\mu\nu} \partial_\mu \Phi \partial_\nu \Phi - 2V(\Phi) - \mathcal{L}(\mathcal{F})), \quad (6)$$

where $\epsilon = +1(-1)$ characterizes the canonical (phantom) scalar field with positive (negative) kinetic energy, which will be fixed later. $\mathcal{L}(\mathcal{F})$ is the Lorentz invariant NED field Lagrangian density with $\mathcal{F} \equiv F_{\mu\nu} F^{\mu\nu}$ as the Faraday invariant defined in terms of the NED field tensor $F_{\mu\nu}$. On varying the action (6) with the metric tensor field $g_{\mu\nu}$ leads to the following gravitational field equations

$$G_{\mu\nu} = T_{\mu\nu} \equiv T_{\mu\nu}^{(\Phi)} + T_{\mu\nu}^{(\text{EM})}, \quad (7)$$

with $T_{\mu\nu}^{(\Phi)}$ and $T_{\mu\nu}^{(\text{EM})}$, respectively, being the EMT for the scalar field and the NED field as follows [100]

$$T_{\mu\nu}^{(\Phi)} = 2\epsilon \partial_\mu \Phi \partial_\nu \Phi - g_{\mu\nu} (\epsilon g^{\alpha\beta} \partial_\alpha \Phi \partial_\beta \Phi - V(\Phi)), \quad (8)$$

$$T_{\mu\nu}^{(\text{EM})} = 2 \left(\frac{\partial \mathcal{L}(\mathcal{F})}{\partial \mathcal{F}} F_{\mu\sigma} F_\nu^\sigma - \frac{1}{4} g_{\mu\nu} \mathcal{L}(\mathcal{F}) \right). \quad (9)$$

Whereas on varying the action with scalar field Φ and $F_{\mu\nu}$, the corresponding dynamical equations read as

$$2\epsilon g^{\mu\nu} \nabla_\mu \nabla_\nu \Phi - \frac{dV(\Phi)}{d\Phi} = 0, \quad (10)$$

$$\nabla_\mu \left(\frac{\partial \mathcal{L}(\mathcal{F})}{\partial \mathcal{F}} F^{\mu\nu} \right) = 0. \quad (11)$$

With the time translational and spherical symmetry of the metric (1), we can make some assumptions about the scalar and NED fields. In particular, we assume that the scalar field Φ is time-independent and function of only spatial coordinates, whereas the NED field Faraday tensor has only two possible nonzero components: $F_{ty} = -F_{yt}$ (a radial electric field) and $F_{\theta\phi} = -F_{\phi\theta}$ (a radial magnetic field). Because of the intrinsic issues in the electric field NED describing a regular black hole spacetime [101], we will take the case of only the magnetic field, such that $F_{\theta\phi} = p \sin \theta$, where p is the magnetic monopole charge. The Faraday invariant takes the form $\mathcal{F} = \frac{2p^2}{(k^2 + y^2)^2}$. Under these assumptions, the EMT becomes

$$T_\mu^{\nu(\Phi)} = \epsilon \frac{y - 2M}{\sqrt{k^2 + y^2}} \Phi'^2 \text{diag}(-1, +1, -1, -1) + \delta_\mu^\nu V(\Phi), \quad (12)$$

$$T_\mu^{\nu(\text{EM})} = \frac{-\mathcal{L}(\mathcal{F})}{2} \text{diag}\left(1, 1, 1 - \frac{4p^2 \mathcal{L}'(\mathcal{F})}{\mathcal{L}(\mathcal{F})(k^2 + y^2)^2}, 1 - \frac{4p^2 \mathcal{L}'(\mathcal{F})}{\mathcal{L}(\mathcal{F})(k^2 + y^2)^2}\right). \quad (13)$$

It is worthwhile to note that neither the scalar field nor the NED field can independently be the source for the LQG-motivated polymerized black hole. The EMT for a scalar field (12) admits $T_t^{t(\Phi)} = T_\theta^{\theta(\Phi)}$ whereas for the NED field, $T_t^{t(\text{EM})} = T_y^{y(\text{EM})}$, but these are not satisfied individually for the polymerized black hole as given in Eqs. (3)-(5). Adopting this approach helps us assess the necessity of including both the NED and scalar fields in the action. However, in what follows, we show that a linear combination of a suitable scalar field and the NED field generates a polymerized black hole.

From Eqs. (12) and (13), the difference of Eqs. (3) and (4) is independent of the NED field, and thus integrating it leads to the scalar field solution

$$\Phi(y) = c_1 \pm \frac{1}{\sqrt{-\epsilon}} \arctan\left(\frac{y}{k}\right), \quad (14)$$

where c_1 is an integration constant. Clearly, $\epsilon = 1$ leads to an unphysical scalar field solution, thus only the phantom scalar field is an acceptable source. Similarly, the difference between the Eqs. (3) and (5) has a contribution only from the NED field, and integrating it yields the NED field Lagrangian density solution

$$\mathcal{L}(\mathcal{F}) = 2 \left(\frac{25k^2 \left(\sqrt{\frac{2p^2}{\mathcal{F}}} - k^2 \right)^{3/2} + 16 \left(\sqrt{\frac{2p^2}{\mathcal{F}}} - k^2 \right)^{5/2} + 18k^4 M}{15k^2 \left(\frac{2p^2}{\mathcal{F}} \right)^{5/4}} + \frac{1}{\sqrt{\frac{2p^2}{\mathcal{F}}}} \right). \quad (15)$$

Using the expressions for scalar field and the NED field Lagrangian density, one can use the field equation to

determine the scalar field potential

$$V(y) = \frac{2(k^4(15y - 6M) + 20k^2y^3 + 8y^5)}{15k^2(k^2 + y^2)^{5/2}}. \quad (16)$$

The polymerized black hole parameter k can be interpreted as the scalar field charge. Thus, the LQG motivated polymerized black hole described by the metric (1) is an exact solution of the Einstein field equations sourced by the minimally coupled phantom scalar field (14) with non-zero potential (16) and the NED field associated with the magnetic field (15).

III. GRAVITATIONAL DEFLECTION OF LIGHT

To study the lensing effects, we adopt the configuration where the black hole L is situated between a point source of light S and an observer O . Both the source and the observer are at distances much larger than the horizon radius, r_+ , from the black hole in the asymptotically flat region. A black hole, by virtue of its strong gravitational field, acts as a *gravitational convex* lens and bends the path of light rays coming from the source [33] (cf. Fig. 2). However, in contrast to an optical convex lens, the amount of deflection experienced by light is inversely proportional to the impact parameter and the distance of the closest approach to the lens center [102]. The presence of the spherical symmetry allows us to fix the plane of motion $\theta = \pi/2$. The two commuting spacetime isometries along Killing vectors $\xi_{(t)}^\mu = \delta_t^\mu$ and $\xi_{(\phi)}^\mu = \delta_\phi^\mu$ lead to two independent constant of motion for photon geodesics, viz., the energy $E = -p_\mu \xi_{(t)}^\mu$ and angular momentum $L = p_\mu \xi_{(\phi)}^\mu$; p^μ is the photon four-momentum [103]. Solving the geodesic equation of motion for test particles ($\delta = 0$ for photon and $\delta = -1$ for massive test particle) yields

$$\dot{t} = -\frac{E}{A(x)}, \quad \dot{\phi} = \frac{L}{C(x)}, \quad (17)$$

with

$$-A(x)\dot{t}^2 + B(x)\dot{x}^2 + C(x)\dot{\phi}^2 = \delta, \quad (18)$$

$$\Rightarrow \dot{x}^2 = \frac{\delta}{B(x)} + \frac{E^2}{A(x)B(x)} - \frac{L^2}{B(x)C(x)}, \quad (19)$$

$$\dot{x}^2 + V_{\text{eff}} = E^2 \quad (20)$$

where $\dot{x}^\mu = \frac{dx^\mu}{d\tau}$ and τ is the affine parameter along the geodesics. We have normalized the coordinates by $2M$, viz., $x = r/2M$, $t = t/2M$ and parameter $k \rightarrow k/2M$. V_{eff} is the radial effective potential. Thus, the photon four-momentum components read as

$$p^\mu = \left(\frac{-E}{A(x)}, \sqrt{\frac{E^2}{A(x)B(x)} - \frac{L^2}{B(x)C(x)}}, 0, \frac{L}{C(x)} \right). \quad (21)$$

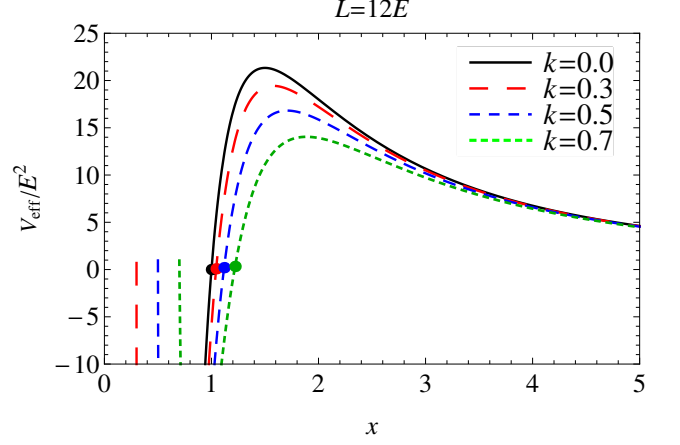


FIG. 1. Comparing the radial effective potential of photons with various k values to that of a Schwarzschild black hole (solid black line). V_{eff} vanishes at asymptotically large distances. For $k \neq 0$, V_{eff} has local minima at $x < x_+$ and maxima at $x > x_+$. The colored points depict the horizon location. For $k \neq 0$, V_{eff} does not vanish at the horizon but rather $V_{\text{eff}}(x_+) < E^2$.

For the sake of the geodesic motion, the relevant quantity is the ratio of L and E , which is called the impact parameter

$$b \equiv \frac{L}{E} = \frac{C(x)\dot{\phi}}{A(x)\dot{t}}, \quad (22)$$

where b is a dimensionless parameter. The radial effective potential and its derivatives with respect to the radial coordinate x for the photon read as

$$V_{\text{eff}} = E^2 - \left(\frac{E^2}{A(x)B(x)} - \frac{L^2}{B(x)C(x)} \right) \quad (23)$$

$$= \frac{E^2 k^2}{x^2} + \frac{L^2}{x^5} \left(x \sqrt{1 - \frac{k^2}{x^2}} - 1 \right) (x^2 - k^2), \quad (24)$$

$$\begin{aligned} V'_{\text{eff}} &= \frac{A'(x)E^2}{A(x)^2 B(x)} + \frac{B'(x)E^2}{A(x)B(x)^2} - \frac{L^2 C'(x)}{B(x)C(x)^2} - \frac{L^2 B'(x)}{B(x)^2 C(x)} \\ &= \frac{k^2 \left(L^2 \left(5x \sqrt{1 - \frac{k^2}{x^2}} - 5 \right) - 2E^2 x^3 \right)}{x^6} \\ &\quad + \frac{L^2 \left(3 - 2x \sqrt{1 - \frac{k^2}{x^2}} \right)}{x^4}. \end{aligned} \quad (25)$$

The geodesic equation (20) determines the fate of a given light ray depending on its impact parameter. From Eq. (20), it is clear that light rays can propagate only in the region with $E^2 \geq V_{\text{eff}}$. Furthermore, being an asymptotically-flat spacetime, we obtain $\lim_{x \rightarrow \infty} V_{\text{eff}} = 0$, thus, the photon can exist at infinity $x \rightarrow \infty$ with $\dot{x}^2 = E^2 \geq 0$.

We assume that the light ray coming from a far distant source gets reflected at the closest distance $x = x_0$ from a

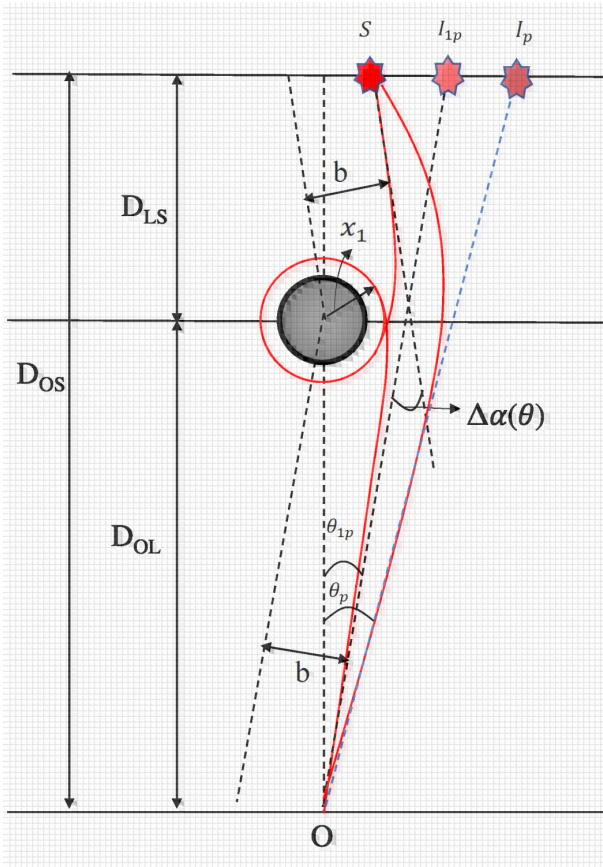


FIG. 2. Schematic for the geometrical configuration of gravitational lensing. S , I_p , and I_{1p} , respectively, are the source position, direct primary image position, and the first relativistic primary image position. Primary images form on the same side of the black hole.

black hole, and it goes to the observer. At the distance of the closest approach, sometimes called as radial turning point radius $x = x_0$, the energy of photons matches with the radial effective potential, such that $V_{\text{eff}} = E^2$ giving $\dot{x} = 0$. Geodesics equations can be recast as follows

$$\begin{aligned} \frac{d\phi}{dx} &= \frac{\dot{\phi}}{\dot{x}} = \frac{L/C(x)}{\sqrt{\left(\frac{E^2}{A(x)B(x)} - \frac{L^2}{B(x)C(x)}\right)}} \\ &= \frac{1}{E\sqrt{\frac{C(x)}{B(x)}\left(\frac{C(x)}{A(x)b^2} - 1\right)}}. \end{aligned} \quad (26)$$

At the distance of closest approach, $\frac{dx}{d\phi} = 0$ or $V_{\text{eff}} = E^2$ in Eq. (23), this yields

$$b_0 = \sqrt{\frac{C_0}{A_0}}, \quad (27)$$

providing that $B(x)$ and $C(x)$ are nonzero at $x \sim x_0 > x_+$. Here and hereafter, all the quantities with subscript “0” are evaluated at $x = x_0$. Because the impact parameter is constant along the geodesics, with

the knowledge of b_0 , we can determine the distance of closest approach x_0 using Eq. (27). In the close vicinity of the black hole horizon, light rays experience strong gravitational deflection and can make close circular orbits, such that $\dot{x} = \ddot{x} = 0$ at $x = x_c > x_+$, which happens for photons having the same energy as the radial potential maximum. $x = x_c$ is the unstable circular photon orbit radius, which can be determined by

$$V_{\text{eff}} = E^2, \quad V'_{\text{eff}} = 0 \quad \text{and} \quad \lim_{x_0 \rightarrow x_c} V_{\text{eff}}(x_0)'' \geq 0,$$

leading to

$$D(x) \equiv \frac{C'(x)}{C(x)} - \frac{A'(x)}{A(x)}, \quad (28)$$

x_c is the largest positive root of $D(x_c) = 0$, obtained as

$$x_c = \frac{1}{2} \sqrt{\frac{3}{2}} \sqrt{4k^2 + 3 + \sqrt{8k^2 + 9}}. \quad (29)$$

In principle, photons can make any number of loops around the black hole and eventually construct a timelike spherical surface known as the photon sphere, which appears as a *critical curve* on the image plane [15]. Light rays with the critical value of impact parameter $b_c = \lim_{x_0 \rightarrow x_c} b(x_0)$ make an infinite number of loops along the unstable circular orbit of critical radius x_c . These orbits are radially unstable, as small radial perturbations drive these photons into the black hole or toward spatial infinity [103]. Indeed, these are the photons that can go closest to the black hole and still escape the black hole and manage to reach a distant observer, therefore, the distance of closest approach is $x_0 \geq x_c$.

The circular photon orbit radius increases with the polymer parameter k , and for $k = 0$, the orbit radius is $x_c = 3/2$. Therefore, b_c is the minimum value of the impact parameter for continuum turning of light geodesics, such that light rays with the impact parameter $b < b_c$ are captured by the black hole, while those with $b > b_c$ are deflected. These captured light rays eventually fall into a black hole and cast the black hole’s *shadow*.

Fig. 1 shows the dimensionless radial effective potential for the light rays around the polymerized black hole. For comparison V_{eff} for the Schwarzschild black hole is also shown. It is evident that $k \neq 0$ causes significant changes in the effective potential. Indeed, the radial effective potential possesses both local maxima and minima, which, respectively, lead to the formation of unstable and stable photon circular orbits. Therefore, in contrast to the Schwarzschild black hole, around a polymerized black hole anti-photon sphere (stable bound orbits) is also possible. These stable photon orbits, however, invariably occur inside the event horizon and hence have no observational value. In what follows, we will discuss gravitational lensing only around the outer photon sphere.

The light rays traveling from the source to an observer suffer the total deflection angle α_D , that is given by [16,

41]

$$\alpha_D(x_0) = I(x_0) - \pi, \quad (30)$$

with

$$\begin{aligned} I(x_0) &= \int_{x_0}^{D_{LS}} \frac{d\phi}{dx} dx + \int_{x_0}^{D_{OL}} \frac{d\phi}{dx} dx \\ &= 2 \int_{x_0}^{\infty} \frac{d\phi}{dx} dx \\ &= \int_{x_0}^{\infty} \frac{2 dx}{\sqrt{\frac{C(x)}{B(x)} \left(\frac{C(x)A(x_0)}{C(x_0)A(x)} - 1 \right)}}. \end{aligned} \quad (31)$$

Here, D_{LS} and D_{OL} are the source and observer distances from the black hole, which in this case can be taken as $D_{LS} \rightarrow \infty$ and $D_{OL} \rightarrow \infty$. It is clear that in the absence of the black hole's gravitational field ($A(x) = B(x) = 1, C(x) = x^2$), the $I(x_0) = \pi$ and deflection angle vanish. We name the limits $x_0 \gtrsim x_c$ and $x_0 \gg x_c$, respectively, as the strong deflection limit and the weak deflection limit.

A. Weak Gravitational Lensing

We begin by analyzing the weak gravitational lensing for light rays with a large impact parameter $b \gg b_c$, such that the closest approach distance x_0 is very large compared to the photon orbit radius x_c . In this case, light rays starting from the source reach the observer without winding around the black hole as the deflection angle is smaller than 2π . Using Eq. (31)

$$I(x_0) = \int_{x_0}^{\infty} \frac{2 dx}{\sqrt{\frac{(x^2 - k^2)(x^3(\sqrt{x_0^2 - k^2} - 1) - x_0^3(\sqrt{x^2 - k^2} - 1))}{xx_0^3}}}. \quad (32)$$

Let us define $y = \frac{x_0}{x}$ and make Taylor series expansion of the integrand in Eq. (32)

$$I(x_0) = \int_0^1 2f(y) dy, \quad (33)$$

with

$$\begin{aligned} f(y) &\sim \frac{1}{\sqrt{1-y^2}} - \frac{(y^3-1)}{2x_0(1-y^2)^{3/2}} \\ &+ \frac{(2k^2(3y^2+1)(y^2-1)^2 + 3(y^3-1)^2)}{8x_0^2(1-y^2)^{5/2}} \\ &- \frac{(y^3-1)(2k^2(5y^2+3)(y^2-1)^2 + 5(y^3-1)^2)}{16x_0^3(1-y^2)^{7/2}} \\ &+ \mathcal{O}\left(\frac{1}{x_0^4}\right). \end{aligned} \quad (34)$$

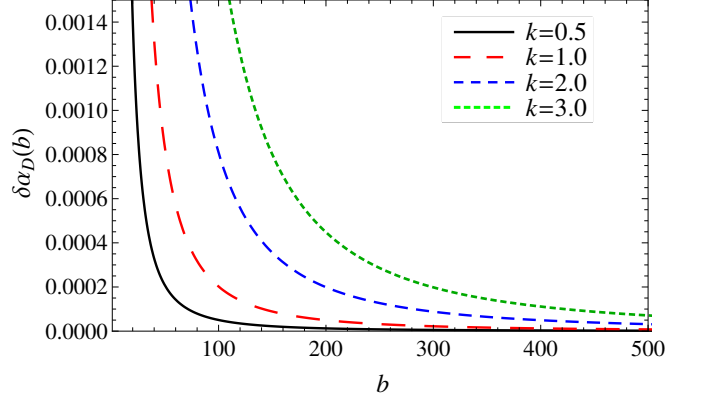


FIG. 3. The correction in the light deflection angle $\delta\alpha_D = \alpha_D - \alpha_D|_{Sch}$ for the polymerized black hole from the Schwarzschild black hole. $\delta\alpha_D$ is in units of radian and b is a dimensionless impact parameter.

Integrating $f(y)$ as in Eq. (33) and using Eq. (30), the deflection angle reads as

$$\begin{aligned} \alpha(x_0) &= \frac{2}{x_0} + \frac{1}{x_0^2} \left(-1 + \frac{15\pi}{16} + \frac{5\pi k^2}{8} \right) \\ &- \frac{1}{x_0^3} \left(\frac{15\pi}{16} - \frac{61}{12} \frac{29k^2}{6} + \frac{5\pi k^2}{8} \right) + \mathcal{O}\left(\frac{1}{x_0^4}\right) \end{aligned} \quad (35)$$

Clearly, the deflection angle inversely depends on the distance of closest approach to the black hole x_0 . Using Eq. (27), we expand the impact parameter in the series of $1/x_0$ and this gives

$$\frac{1}{x_0} = \frac{1}{b} + \frac{1}{2b^2} + \frac{5+2k^2}{8b^3} + \mathcal{O}\left(\frac{1}{b^4}\right). \quad (36)$$

Inserting the above expression in Eq. (35), we obtain

$$\begin{aligned} \alpha_D(u) &= \frac{4M}{u} + \frac{4M^2}{u^2} \left(\frac{15\pi}{16} + \frac{5\pi k^2}{8} \right) + \frac{128M^3(1+k^2)}{3u^3} \\ &+ \mathcal{O}\left(\frac{1}{u^4}\right), \end{aligned} \quad (37)$$

where $u = 2Mb$ is the re-scaled impact parameter with dimension of length. For the limit $k \rightarrow 0$, the Eq. (37) recovers the deflection angle for the Schwarzschild black hole, which reads as [15, 41]

$$\alpha_D(u)|_{Sch} = \frac{4M}{u} + \frac{15\pi M^2}{4u^2} + \frac{128M^3}{3u^3} + \mathcal{O}\left(\frac{1}{u^4}\right). \quad (38)$$

It is clear that quantum effects, by virtue of polymer quantization, contribute positively to the deflection angle, viz., polymerized black hole produces a larger deflection angle than the Schwarzschild black hole even in the weak-deflection limit. The primary quantum correction to the weak deflection angle is of the order of u^{-2} . Fig. 3 depicts this correction in the deflection

angle; $\delta\alpha_D$ is more significant for smaller values of b . However, Fig. 3 gives the correct description only for $b \gg b_c$. For $b = 500$, the correction in polymerized black hole deflection angle with $k = 0.5$ is 0.4072 milli-arc-seconds.

B. Strong Gravitational Lensing

As the distance of minimum approach x_0 decreases, the deflection angle increases and eventually diverges (cf. from Eq. (35)). However, to get the correct order of divergence for the strong gravitational lensing, we shall expand the deflection angle near the photon sphere $x_0 \sim x_c$. For this purpose, we define a new variable z as in Ref. [47]

$$z = 1 - \frac{x_0}{x}. \quad (39)$$

It is worth noting here that an alternate choice of z can also be made, such as $z = \frac{A(x)-A(x_0)}{1-A(x_0)}$, as discussed by Bozza in Ref. [16]. However, the advantage of adopting the choice in Eq. (39) is that it is equally valid for ultra static spacetime (such as wormhole) with constant $A(x)$. Secondly, for other choices of z , it is not always possible to obtain the analytic expressions of deflection angle in the strong deflection limit [48].

Using Eq. (39), the integral in Eqs. (31) and (32) can be re-written as

$$I(x_0) = \int_0^1 f(z, x_0) dz, \quad (40)$$

with the function

$$f(z, x_0) = \frac{2x_0}{(1-z)^2} \frac{1}{\sqrt{\frac{C(x)}{B(x)} \left(\frac{C(x)A(x_0)}{C(x_0)A(x)} - 1 \right)}}. \quad (41)$$

Inserting metric functions for the polymerized black hole and $x = \frac{x_0}{1-z}$, this leads to

$$\begin{aligned} f(z, x_0) &= 2x_0^{3/2} \left\{ (k^2(z-1)^2 - x_0^2) \left(-\sqrt{x_0^2 - k^2} \right. \right. \\ &\quad \left. \left. + \sqrt{x_0^2 - k^2(z-1)^2} + z \left(3 - 2\sqrt{x_0^2 - k^2(z-1)^2} \right. \right. \right. \\ &\quad \left. \left. \left. + z(z-3 + \sqrt{x_0^2 - k^2(z-1)^2}) \right) \right) \right\}^{-1/2} \\ &\equiv \frac{2x_0}{\sqrt{G(z, x_0)}}. \end{aligned} \quad (42)$$

Making the Taylor series expansion of the integrand $G(z, x_0)$ yields

$$G(z, x_0) = \sqrt{\phi_1 z + \phi_2 z^2 + \mathcal{O}(z^3)}, \quad (43)$$

with

$$\begin{aligned} \phi_1 &= \frac{x_0 \left(C'(x_0)A(x_0) - A'(x_0)C(x_0) \right)}{A(x_0)B(x_0)}, \\ \phi_2 &= \frac{-x_0}{B(x_0)} \left(3C'(x_0) - \frac{x_0 C''(x_0)}{2} + \frac{x_0 C'(x_0)B'(x_0)}{B(x_0)} \right) \\ &\quad + \frac{x_0^2 C'^2(x_0)}{B(x_0)C(x_0)} + \frac{3x_0 C(x_0)}{A(x_0)B(x_0)} \left(A'(x_0) - \frac{x_0 A''(x_0)}{6} \right) \\ &\quad - \frac{x_0^2 C(x_0)A'(x_0)}{A(x_0)B(x_0)} \left(\frac{2C'(x_0)}{C(x_0)} - \frac{A'(x_0)}{A(x_0)} - \frac{B'(x_0)}{B(x_0)} \right). \end{aligned} \quad (44)$$

For the polymerized black hole, these coefficients take the form

$$\begin{aligned} \phi_1 &= -3x_0 + 2x_0 \sqrt{x_0^2 - k^2} + \frac{3k^2}{x_0} (1 - \sqrt{x_0^2 - k^2}), \\ \phi_2 &= 3x_0 - \frac{9k^2}{x_0} + \frac{(18k^4 + 17k^2 x_0^2 - 2x_0^4)}{2x_0 \sqrt{x_0^2 - k^2}}. \end{aligned} \quad (45)$$

In the strong deflection limit $x_0 \rightarrow x_c$, from Eqs. (28) and (44)

$$\begin{aligned} \phi_1 &\rightarrow 0, \\ \phi_2 &\rightarrow \frac{x_c^2 C(x_c)}{2B(x_c)} \left(\frac{C''(x_c)}{C(x_c)} - \frac{A''(x_c)}{A(x_c)} \right). \end{aligned} \quad (46)$$

Therefore, in the limit $x_0 \rightarrow x_c$, the leading order of the divergence of the integrand term $f(z, x_0)$ is z^{-1} and that the integral $I(x_0)$ and deflection angle diverge logarithmically, i.e., $\alpha_D \propto \log(z) \propto \log(1 - \frac{x_c}{x})$ (cf. Eq. (42)). It is the reason why we truncate the Taylor series expansion in Eq. (43) at z^2 . The sole idea is to identify the diverging term and order of divergence, so that the diverging term can be subtracted from $I(x_0)$ to get the regular term $I_R(x_0)$. Dividing the integral $I(x_0)$ into two parts, diverging $I_D(x_0)$ and regular $I_R(x_0)$, the $I_D(x_0)$ reads as

$$I(x_0) = I_D(x_0) + I_R(x_0), \quad (47)$$

$$f(z, x_0) = f_D(z, x_0) + f_R(z, x_0), \quad (48)$$

$$I_D(x_0) = \int_0^1 \frac{2x_0 dz}{\sqrt{\phi_1 z + \phi_2 z^2}}. \quad (49)$$

Upon integration, the diverging term contribution reads as

$$I_D(x_0) = \frac{4x_0}{\sqrt{\phi_2}} \log \left(\frac{\sqrt{\phi_2} + \sqrt{\phi_1 + \phi_2}}{\sqrt{\phi_1}} \right). \quad (50)$$

Expanding ϕ_1 in the close vicinity of x_c

$$\begin{aligned} \phi_1 &= \frac{x_c C(x_c)}{B(x_c)} \left(\frac{C''(x_c)}{C(x_c)} - \frac{A''(x_c)}{A(x_c)} \right) (x_0 - x_c) \\ &\quad + \mathcal{O}((x_0 - x_c)^2). \end{aligned} \quad (51)$$

To get the coordinate independent expression of the deflection angle, we express it in terms of the impact

parameter. For this purpose, using Eq. (27) and making a Taylor expansion around $x_0 \sim x_c$, we get

$$b(x_0) = \sqrt{\frac{C(x_c) + (x_0 - x_c)C'(x_c) + \frac{1}{2}(x_0 - x_c)^2 C''(x_c)}{A(x_c) + (x_0 - x_c)A'(x_c) + \frac{1}{2}(x_0 - x_c)^2 A''(x_c)}},$$

$$b(x_0) = b(x_c) + \frac{(x_0 - x_c)^2}{4} \sqrt{\frac{C(x_c)}{A(x_c)} \left(\frac{C''(x_c)}{C(x_c)} - \frac{A''(x_c)}{A(x_c)} \right)} + \mathcal{O}((x_0 - x_c)^2). \quad (52)$$

Upon eliminating $(x_0 - x_c)$ from Eq. (51) and using Eq. (52), the coefficient ϕ_1 in the $x_0 \rightarrow x_c$ reads as

$$\phi_1 = \frac{2C(x_c)x_c}{B(x_c)} \left(\frac{C''(x_c)}{C(x_c)} - \frac{A''(x_c)}{A(x_c)} \right)^{1/2} \left(\frac{b}{b_c} - 1 \right)^{\frac{1}{2}}. \quad (53)$$

Substituting Eqs. (46) and (53) into (50), we obtain the divergent part $I_D(b)$ of the deflection angle in the strong deflection limit [47]

$$I_D(b) = \frac{x_c}{\sqrt{\phi_2}} \log x_m^2 \left(\frac{C''(x_c)}{C(x_c)} - \frac{A''(x_c)}{A(x_c)} \right) - \frac{x_c}{\sqrt{\phi_2}} \log \left(\frac{b}{b_c} - 1 \right) + \mathcal{O}((b - b_c) \log(b - b_c)). \quad (54)$$

To determine the regular part in the deflection angle Eq. (47), we first make the Taylor series expansion of $f_R(z, x_0)$ around $x_0 \sim x_c$ and then integrate.

$$I_R(x_c) \equiv \int_0^1 f_R(z, x_c) dz. \quad (55)$$

This integration can be done analytically, however, it results in a long and complicated expression for the polymerized black hole. Here, we completed our deflection angle calculation, which can be rewritten in a compact form as follows [47]

$$\alpha_D(u) = -\bar{p} \log \left(\frac{u}{u_c} - 1 \right) + \bar{q} + \mathcal{O}((u - u_c) \log(u - u_c)), \quad (56)$$

where \bar{p} and \bar{q} are given by

$$\bar{p} = \sqrt{\frac{2B(x_c)A(x_c)}{C''(x_c)A(x_c) - C(x_c)A''(x_c)}} \quad (57)$$

and

$$\bar{q} = \bar{p} \log \left[x_c^2 \left(\frac{C''(x_c)}{C(x_c)} - \frac{A''(x_c)}{A(x_c)} \right) \right] + I_R(x_c) - \pi, \quad (58)$$

respectively, where $I_R(x_c)$ is given by the Eq. (55). Here, \bar{p} and \bar{q} are called the strong deflection limit coefficients. Contribution from the regular part is in the \bar{q} expression. Therefore, in the strong deflection limit $x \rightarrow x_c$ or $b \rightarrow b_c$, the deflection angle diverges logarithmically (cf. Eq. (56)). Strong lensing observables are characterized

by the coefficients \bar{p} and \bar{q} , therefore, it is important to get the exact expression of \bar{p} and \bar{q} , as they might give us a hint to understand relations between the gravitational lensing and other phenomena in the strong gravitational fields [47].

It is interesting to find the value of the impact parameter with which light rays make n complete loops around the black hole with a deflection angle $\alpha_D = 2\pi n$. Inverting the relation in Eq. (56), the corresponding value of impact parameter reads

$$u_n = u_c \left(1 + e^{\left(\frac{\bar{q} - 2\pi n}{\bar{p}} \right)} \right). \quad (59)$$

It is clear that for large n , impact parameters exponentially approach the critical value with which light rays make an infinite winding around the black hole. For instance, light rays moving around a polymerized black hole with $k = 0.10$ make the first three complete loops for impact parameters u_n and orbit radii x_n as $u_1 = 6.61319$, $u_2 = 6.60633$, $u_3 = 6.60632071$ and $x_1 = 2.09412$, $x_2 = 2.04447$, $x_3 = 2.042342927$, whereas $u_c = 6.60632069$ and $x_c = 2.0423429216$.

Fig. 4 depicts the lensing coefficients as a function of k . Both \bar{p} and \bar{q} decrease with k , and for $k = 0$ they smoothly retain the values for the Schwarzschild black hole, viz., $\bar{p} = 1$ and $\bar{q} = -0.4002$ [15, 16]. In Fig. 5 (left figure), the deflection angle $\alpha_D(u)$ is shown as a function of impact parameter u for various values of k . Deflection angle decreases with impact parameter and only for $u = u_c$ deflection angle shows divergence. The direct effect of k on the deflection angle $\alpha_D(u)$ is shown in Fig. 5 (right figure), where we fixed the light impact parameter and plotted $\alpha_D(u)$ as a function of k . $\alpha_D(u)$ increases with k . Therefore, the deflection angle is higher for the polymerized black holes than for the Schwarzschild black holes. Because the amount of deflection of light rays varies with the k , the light density received by the distant observers will be different, which naturally leads to the different observation intensity caused by the black hole shadow, as we will see in the next section. In Fig. 6, we plotted the deflection angle analytically calculated in the weak (37) and strong (56) field limits as a function of u for $k = 0.50$ and compared it with the exact deflection angle calculated numerically using (30). The strong deflection angle is an excellent approximation for photons passing close to the photon sphere.

IV. LENSING OBSERVABLES

We consider that the source and the observer are on opposite sides of the black hole, as shown in the lensing setup in Fig. 2. Here, $D_{SO} = D_{SL} + D_{LO}$ is the distance between observer and source. All distances are measured along the optical axis, and they are taken much larger than the horizon radius. The line joining the observer and the black hole is considered a reference optical axis

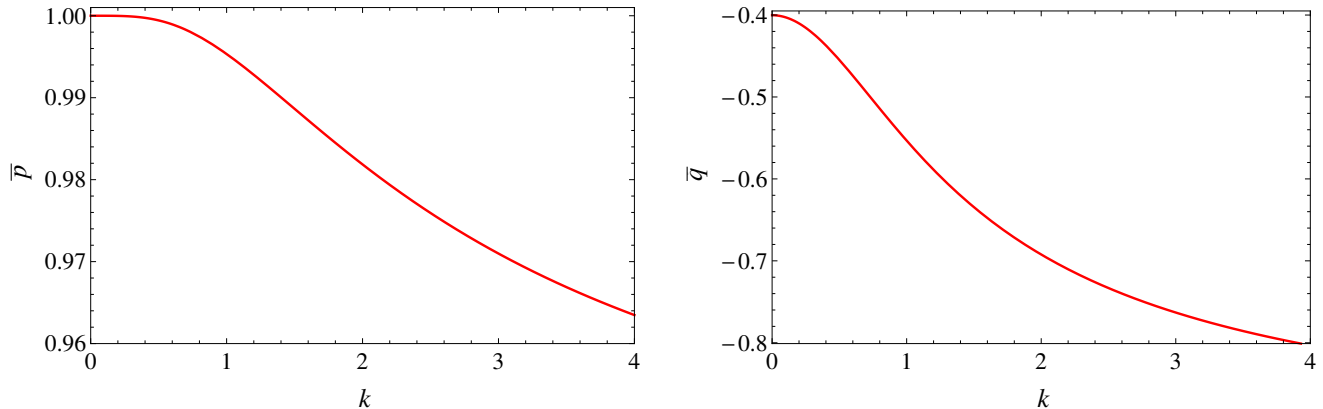


FIG. 4. The behavior of strong lensing coefficients \bar{p} and \bar{q} as a function of k .

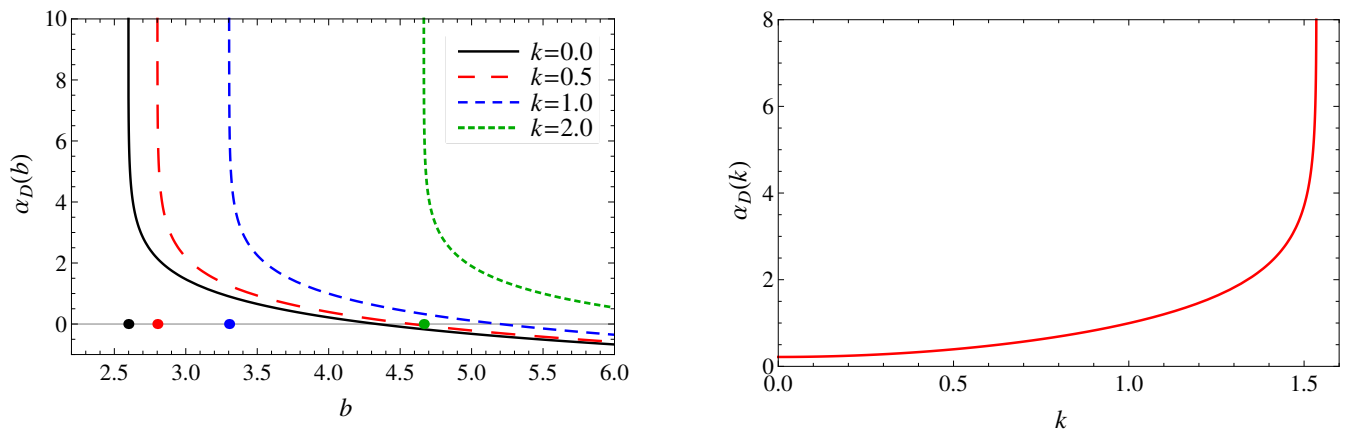


FIG. 5. (Left:) The variation of deflection angle as a function of impact parameter b for different values of k . The points on the horizontal axis correspond to the impact parameter $b = b_c$ at which the deflection angle diverges logarithmically. α_D is in units of radians. (Right:) Deflection angle variation with k for $b = 4$.

and all the angles, θ (image position) and β (source position), are measured with respect to this axis at the observer position.

Light rays traveling from the source to the observer are deflected, near a black hole, from their original path by an angle α_D and thus the observer sees the image of the source at the angular position θ , which is different from the source position β . The lens equation establishes the relation between the image position and the source position in terms of the deflection angle by the following relation [16, 41, 45]

$$D_{OS} \tan \beta = \frac{D_{OL} \sin \theta - D_{LS} \sin(\alpha_D - \theta)}{\cos(\alpha_D - \theta)}. \quad (60)$$

This equation is known as the Virbhadrā–Ellis lens equation [41]. As shown in the previous section, in the strong deflection limit, light can make $n \in \mathbb{N}$ numbers of loops around the black hole before escaping to the observer, and the effective deflection angle can be defined as the $\bar{\alpha}_D = \alpha_D - 2\pi n$, such that $2\pi n$ is the

deflection angle for the n complete loops. All the angles in Eq. (60) should be within $(0, 2\pi)$ and thus we shall use the deflection angle $\bar{\alpha}_D$ rather α_D . We assume that the source and images are close to the optical axis, thereby in the small-angle limit, $\beta \ll 1, \theta = b/D_{OL} \ll 1$, expectedly deflection angle is also small $\bar{\alpha}_D \ll 1$ and Eq. (60) reduces to the following form [45, 104]

$$\epsilon \beta = \theta - \epsilon \frac{D_{LS}}{D_{OS}} \bar{\alpha}_D. \quad (61)$$

It is worth mentioning here that, contrary to most of the earlier studies, we did not assume that the observer and the source are equidistant from the black hole. Here, ϵ takes the values $+1$ or -1 , respectively, describing the direction of light propagation around the black hole. For $\epsilon = +1(-1)$, light rays cross from the front side (backside) of the black hole, and the resulting images appear on the same side (opposite side) of the optical axis with respect to the source. These images are called as the primary ($\epsilon = 1$) and secondary ($\epsilon = -1$) images.

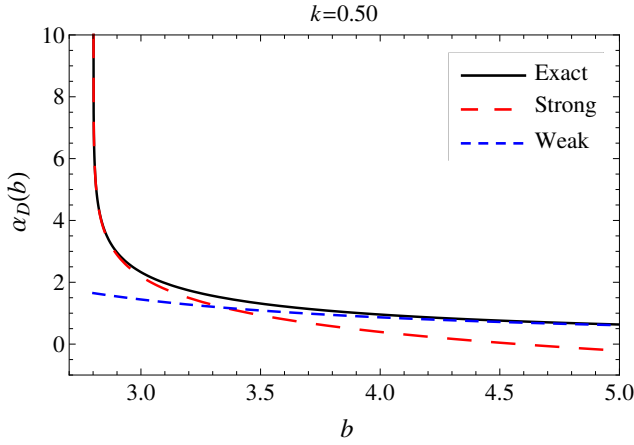


FIG. 6. Comparison of the exact numerical deflection angle (black solid line) with the approximate deflection angle in the strong (red dashed line) and weak (blue small dashed line) field limits. For this case, the critical impact parameter is $b_c = 2.8012$. α_D is in units of radians.

For $b \ll b_c$ the deflection angle is always smaller than 2π and the resulting images are called *direct images*, whereas if the impact parameter is close to its critical value, then photons can make several loops around the black hole before escaping to the observer, such photons make higher-order images, commonly known as *relativistic images*, as introduced by Virbhadra and Ellis [41, 105]. It is important to note that, while there are multiple relativistic images on one side of the optical axis, there can be only one primary image that forms due to light deflection in the weak-field without looping of the light ray around the lens [105]. These direct and relativistic images form on both the same and opposite sides of the source, which are characterized by the value of ϵ . Hereafter, we use subscripts p and s , respectively, for primary and secondary images. Similarly, θ_p and θ_s defines, respectively, *direct* primary and secondary images with zero winding around the black hole, whereas, θ_{np} and θ_{ns} stand, respectively, for the *relativistic* primary and secondary images of order n . The $n \in \mathbb{N}$ is the light rays winding number around the black hole and determines the order of the relativistic images with position θ_n , such that $n = 1$ corresponds to the outermost relativistic image.

To obtain the image position, the scheme is to first calculate the deflection angle α_D in terms of the impact parameter and then express it in terms of θ using $\theta = b/D_{OL}$ and substitute in Eq. (61). Then, for a given angular position of the source β , we solve the lens Eq. (61) for the image position θ . Expanding the deflection angle about (θ_n^0) to the first order [47]

$$\alpha_D(\theta_n) = \alpha_D(\theta_n^0) + \left. \frac{\partial \alpha_D(\theta_n)}{\partial \theta} \right|_{\theta_n^0} (\theta_n - \theta_n^0) + \mathcal{O}(\theta_n - \theta_n^0)^2, \quad (62)$$

where θ_n^0 and $\alpha_D(\theta_n^0) = 2\pi n$ are the image position, and the deflection angle for the light rays making exactly n complete loops around the black hole. Using $\theta = b/D_{OL}$ in the deflection angle Eq. (56) [47]

$$\theta_n^0 = \theta_\infty \left(1 + e^{\frac{\bar{q}-2\pi n}{\bar{p}}} \right), \quad (63)$$

where $\theta_\infty = b_c/D_{OL}$ is the critical curve or photon sphere angular radius. Clearly, the relativistic image angular position θ_n^0 rapidly decrease with n and eventually approach the photon sphere, $\theta_n^0 \rightarrow \theta_\infty$, as the $n \rightarrow \infty$. Differentiating deflection angle with respect to θ in Eq. (56)

$$\left. \frac{\partial \alpha_D(\theta_n)}{\partial \theta} \right|_{\theta_n^0} = -\frac{\bar{p}}{\theta_n^0 - \theta_\infty}, \quad (64)$$

and substituting it in Eq. (62) gives

$$\begin{aligned} \bar{\alpha}_D &= \alpha_D(\theta_n) - \alpha_D(\theta_n^0) = -\frac{\bar{p}(\theta_n - \theta_n^0)}{\theta_n^0 - \theta_\infty} \\ &= -\frac{\bar{p}(\theta_n - \theta_n^0)}{\theta_\infty e^{\frac{\bar{q}-2\pi n}{\bar{p}}}}. \end{aligned} \quad (65)$$

This gives the excess in deflection angle to the $2\pi n$ for the light rays making n complete loops around the black hole. Angular position of the n^{th} relativistic image can be determined by solving Eq. (61) for θ and keeping only lowest order terms in θ_∞ [16]

$$\begin{aligned} \theta_n &= \frac{\epsilon D_{LS} \bar{p} \theta_n^0 + \epsilon D_{OS} \beta \theta_\infty e^{\frac{\bar{q}-2\pi n}{\bar{p}}}}{\epsilon D_{LS} \bar{p} + D_{OS} \theta_\infty e^{\frac{\bar{q}-2\pi n}{\bar{p}}}}, \\ \theta_n &\approx \epsilon \theta_n^0 + (\beta - \epsilon \theta_n^0) \frac{D_{OS} \theta_\infty}{D_{LS} \bar{p}} e^{\frac{\bar{q}-2\pi n}{\bar{p}}}. \end{aligned} \quad (66)$$

This defines the first lensing observables. The correction to θ_n^0 , given in the second term, falls very rapidly with the winding number. Interestingly, for the $b_c \ll D_{OL}$, θ_n is not sensitive to the source position and is mainly defined by θ_n^0 . One particularly interesting case is $\beta = 0$, viz., perfect alignment of the source, black hole, and observer. In this case, the light that starts off from the source can reach the observer from all possible directions, and a point-like source appears as a circular ring, known as the Einstein ring [44, 52]. The angular radii of the n^{th} relativistic Einstein ring can be obtained as $\beta \rightarrow 0$

$$\begin{aligned} \theta_n^E &= \left(1 - \frac{D_{OS} \theta_\infty}{D_{LS} \bar{p}} e^{\frac{\bar{q}-2\pi n}{\bar{p}}} \right) \theta_n^0, \\ &= \theta_\infty \left(1 - \frac{D_{OS} \theta_\infty}{D_{LS} \bar{p}} e^{\frac{\bar{q}-2\pi n}{\bar{p}}} \right) \left(1 + e^{\frac{\bar{q}-2\pi n}{\bar{p}}} \right). \end{aligned} \quad (67)$$

Whereas for the non-zero value of β , the Einstein ring gets broken, and we get multiple images. The primary images are always outside the Einstein ring, $\theta_{np} \geq \theta_E$, while the secondary images are always inside the ring, $\theta_{ns} \leq \theta_\infty$. Both sets of images approach the Einstein ring as $\beta \rightarrow 0$, merging into a single degenerate ring image

with radius θ_E for $\beta = 0$. As β increases primary images move away from the optical axis, whereas secondary images move towards the optical axis. Thus, in principle, a black hole produces two infinite sequences of relativistic images whose positions can be calculated numerically using Eq. (66). The deflection angle calculated for the weak deflection limit in Eq. (37) together with the lens equation (61) is suitable for determining the direct primary and secondary image positions, which reads as [105]

$$\theta_{p,s} = \frac{1}{2} \left(\beta + \epsilon \sqrt{\beta^2 + \frac{8D_{LS}}{D_{OL}D_{OS}}} \right). \quad (68)$$

Another, important lensing observable is the angular separation between the photon sphere and the outermost relativistic image, which is given by [16]

$$\begin{aligned} s &\equiv \theta_1 - \theta_\infty \approx \theta_1^0 - \theta_\infty^0 \\ &= \theta_\infty e^{\frac{\bar{q}-2\pi}{\bar{p}}}. \end{aligned} \quad (69)$$

The significance of s , which is the value to compare with the observation's resolution in order to distinguish amongst a group of relativistic images, is that it is independent of the source position β . Another effect of gravitational lensing is the so-called magnification effect. The ratio of the image flux (product of its surface brightness and the solid angle it subtends on the sky) to the unlensed source flux is known as the image magnification. However, according to Liouville's theorem, gravitational lensing preserves the surface brightness. Therefore, the image magnification turns out to be the ratio of the solid angles of the image and of the unlensed source made at the observer

$$\mu = \frac{\sin \theta}{\sin \beta} \frac{d\theta}{d\beta} \equiv \mu_t \mu_r, \quad (70)$$

$$\mu_n = \frac{\theta_\infty^2 D_{OS} e^{\frac{\bar{q}-2\pi n}{\bar{p}}}}{\beta \bar{p} D_{LS}} \left(\theta_n^0 + \frac{D_{OS} \theta_\infty e^{\frac{\bar{q}-2\pi n}{\bar{p}}}}{D_{LS} \bar{p}} (\beta - \theta_n^0) \right), \quad (71)$$

$$\mu_n \approx \frac{\theta_\infty^2 D_{OS} e^{\frac{\bar{q}-2\pi n}{\bar{p}}} \left(1 + e^{\frac{\bar{q}-2\pi n}{\bar{p}}} \right)}{\beta \bar{p} D_{LS}} + \mathcal{O} \left(\frac{\theta_\infty^3}{D_{LS}^2} \right). \quad (72)$$

Here, $\mu_t = \frac{\sin \theta}{\sin \beta}$ and $\mu_r = \frac{d\theta}{d\beta}$ are the tangential and radial magnifications, respectively. Divergence of tangential (radial) magnification is called tangential (radial) caustic. Quite evidently, Einstein rings ($\beta = 0$) correspond to the tangential caustic. Equation (72) infers that the magnification is very faint unless the lens and the source are highly aligned, and then it linearly diverges for the perfect alignment as in the Einstein ring. Secondly, as expected, the first relativistic image is the brightest one and μ falls rapidly for the higher-order relativistic images. Therefore the outermost set of images, one on each side of the optic axis, is observationally the most significant. The sum of magnification of all the images

can be calculated as [16, 46]

$$\mu = \sum_{n=1}^{\infty} \mu_n = \frac{\theta_\infty^2 D_{OS} \left(1 + e^{\frac{2\pi}{\bar{p}}} + e^{\frac{\bar{q}}{\bar{p}}} \right) e^{\frac{\bar{q}}{\bar{p}}}}{\beta \bar{p} D_{LS} \left(e^{\frac{4\pi}{\bar{p}}} - 1 \right)}. \quad (73)$$

The lensing observable is the ratio of the magnifications of the outermost image to the sum of the other images, which can be calculated using Eqs. (72) and (73) [16, 46]

$$r_{mag} = \frac{\mu_1}{\sum_{n=2}^{\infty} \mu_n} \quad (74)$$

$$\approx \frac{\left(e^{\frac{4\pi}{\bar{p}}} - 1 \right) \left(e^{\frac{2\pi}{\bar{p}}} + e^{\frac{\bar{q}}{\bar{p}}} \right)}{e^{\frac{2\pi}{\bar{p}}} + e^{\frac{4\pi}{\bar{p}}} + e^{\frac{\bar{q}}{\bar{p}}}}. \quad (75)$$

The magnification observable r_{mag} is independent of the source position rather solely depends on the metric parameters through the lensing coefficients \bar{p} and \bar{q} .

Gravitational lensing also leads to a time delay in image formation. Light rays forming the second relativistic image travel $2\pi u_2$ additional distance through their journey from source to observer. This excess path leads to a finite time lag between the formation of the first and second relativistic images, i.e., the second relativistic image forms $\delta t_{12} = 2\pi u_2$ time later than the first image. Similarly, the time difference between the direct secondary and primary images is due to the different paths traveled by photons, it can be calculated as follows [38]

$$\Delta t_{ps} = 4 \left(\frac{\theta_s^2 - \theta_p^2}{2|\theta_p \theta_s|} + \log \left| \frac{\theta_s}{\theta_p} \right| \right). \quad (76)$$

Direct secondary image forms after Δt_{ps} time of the primary image formation. It is important to note that for $\beta = 0$, the direct primary and secondary images form at the same angular distance from optical axis, i.e. $\theta_s = \theta_p$, therefore, time delay vanishes. In addition, the time delay between the images is a useful observable quantity only in the case of transient sources.

V. LENSING BY SUPERMASSIVE BLACK HOLES

We model two astrophysically important supermassive black holes Sgr A* and M87*, residing at the center of Milky-Way and nearby M87 galaxy, as the polymerized black hole and calculate the image positions and lensing observables. We consider, for Sgr A* black hole $M = 4.3 \times 10^6 M_\odot$ and $D_{OL} = 8.35 \times 10^3$ pc [106], and for M87* black hole $M = 6.5 \times 10^9 M_\odot$ and $D_{OL} = 16.8$ Mpc [18]. Fig. 7 depicts the variation in direct primary and secondary images positions with β and k , which is valid in the weak deflection angle limit. The primary (secondary) image always forms outside (inside) the Einstein ring. Although, the primary image position moves farther and farther away from the optical axis with increasing β , it

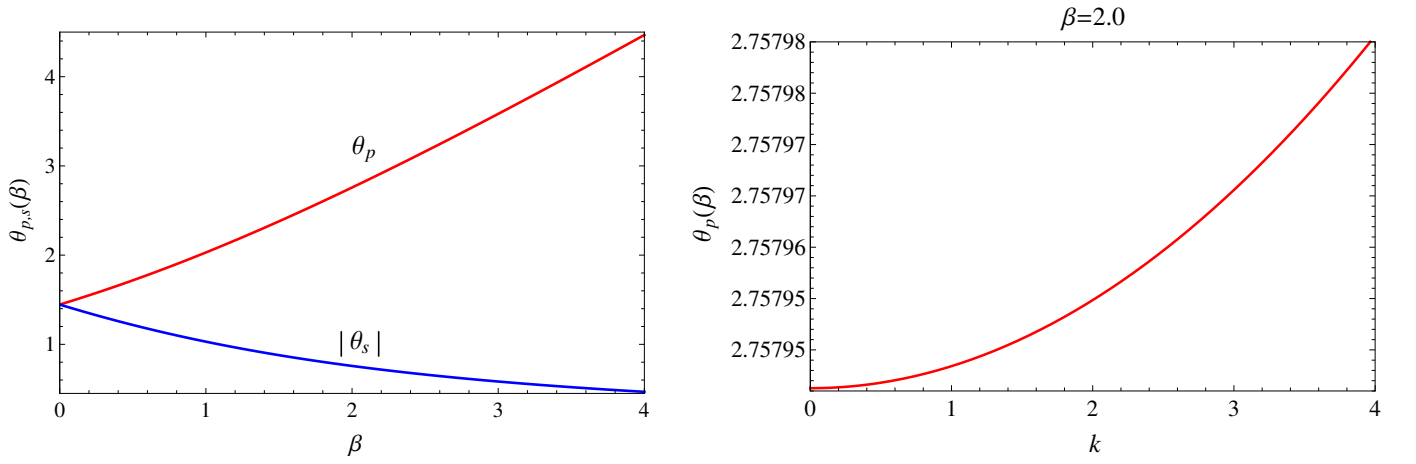


FIG. 7. (Left:) The angular position of the direct primary and secondary images $\theta_{p,s}$ varying with source position β for $k = 1$. (Right:) The angular position of the direct primary image θ_p varying with k for $\beta = 2as$. All angles are in units of $\mathcal{O}(as)$.

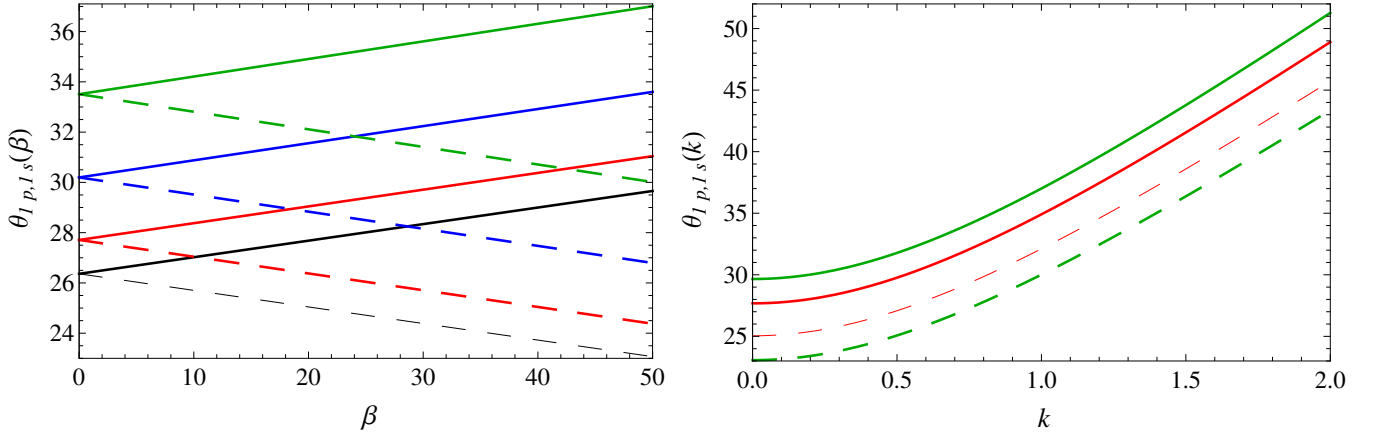


FIG. 8. (Left:) The angular position of the first relativistic primary image θ_{1p} (solid lines) and the secondary image $|\theta_{1s}|$ (dashed lines) varying with source position β for $k = 0$ (black lines), $k = 0.4$ (red lines), $k = 0.7$ (blue lines) and $k = 1.0$ (green lines). (Right:) Angular positions of the first relativistic primary images θ_{1p} and secondary images $|\theta_{1s}|$ (dashed lines) varying with k for $\beta = 20$ as (red lines) and for $\beta = 50$ as (green lines). β is in units of $\mathcal{O}(as)$ and image positions θ are in units of $\mathcal{O}(\mu as)$.

weakly depends on k . The secondary image moves toward the optical axis with increasing β , such that the angular separation between the primary and secondary image increases with β . Table. I and II summarizes the angular position and magnification of direct image ($\theta_{p,s}, \mu_{p,s}$) and the time delay Δt_{ps} between the secondary and primary images for the Sgr A* and M87* black holes. Numerical comparison with the $k = 0$ case suggests that for the polymerized black hole the direct images form farther away compared to the Schwarzschild black hole. Direct images magnifications weakly depend on k but sharply fall with β . The angular position for direct images is of $\mathcal{O}(as)$ whereas the time delay is in minutes and hours for Sgr A* and M87* black holes, respectively. Time delay has weak dependence over k and increases slowly with it.

For the strong gravitational lensing, the first

relativistic primary and secondary image positions are shown and compared with the Schwarzschild black hole in Fig. 8. Angular position of relativistic images is of $\mathcal{O}(\mu as)$ and increases with k . It might be easy to distinguish the direct image from the rest of the relativistic images, which are rapidly converging to the θ_∞ . The relativistic image position, magnification, Einstein ring size, and lensing observables are calculated for Sgr A* and M87* black holes and shown in tables. III and IV, respectively. As expected, the relativistic images are much fainter compared to the direct images, and magnification decreases with the increasing source position. In addition, secondary images are demagnified than the primary images. The Einstein ring size is of $\mathcal{O}(\mu as)$ and it grows with increasing values of k . The separation observable s also increases with k , suggesting

k	β	$\theta_p(\text{as})$	$\theta_s(\text{as})$	μ_p	μ_s	$\Delta t_{ps}(\text{min})$
0	0	1.4458	-1.4458	2.2×10^{15}	-2.2×10^{15}	0
0	10^{-6}	1.445817	-1.445801	722905	-722904.	3.1×10^{-5}
0	10^{-3}	1.446317	-1.445302	723.405	-722.405	0.00197755
0	10^{-1}	1.496681	-1.396666	7.74201	-6.74201	0.194915
0	1	2.029830	-1.029815	1.34662	-0.34662	1.98668
0	3	3.583356	-0.583341	1.02722	-0.027223	6.76852
0	5	5.387970	-0.387954	1.00521	-0.005211	13.4364
2	10^{-6}	1.445837	-1.445781	722905	-722904.	1.08×10^{-4}
2	10^{-3}	1.446336	-1.445282	723.405	-722.405	0.002055
2	10^{-1}	1.496700	-1.396645	7.742	-6.742	0.194992
2	1	2.029843	-1.029788	1.34662	-0.346617	1.98678
2	3	3.583362	-0.583306	1.02722	-0.027222	6.76888
2	5	5.387972	-0.387917	1.00521	-0.005211	13.4374
4	10^{-6}	1.445897	-1.445721	722905	-722904.	3.41×10^{-4}
4	10^{-3}	1.446396	-1.445222	723.405	-722.405	0.0022877
4	10^{-1}	1.496757	-1.396583	7.74199	-6.74199	0.195226
4	1	2.029883	-1.029709	1.34661	-0.346608	1.98708
4	3	3.583378	-0.583204	1.02722	-0.027218	6.76993
4	5	5.387980	-0.387806	1.00521	-0.005210	13.4407

TABLE I. Direct image positions, their magnifications, and the time delay between secondary and primary images for the supermassive black hole Sgr A* for different values of k and β in the weak deflection limit. All angles are in as, and the time delay is in units of minutes.

k	β	$\theta_p(\text{as})$	$\theta_s(\text{as})$	μ_p	μ_s	$\Delta t_{ps}(\text{hrs})$
0	0	1.2532	-1.2532	2.2×10^{15}	-2.2×10^{15}	0
0	10^{-6}	1.253211	-1.253199	626603.	-626602.	0.000691
0	10^{-3}	1.253710	-1.252699	627.102	-626.102	0.057268
0	10^{-1}	1.304207	-1.204196	6.78097	-5.78097	5.66552
0	1	1.849271	-0.849259	1.26728	-0.26727	58.1032
0	3	3.454617	-0.454605	1.01762	-0.01762	204.469
0	5	5.296520	-0.296509	1.00314	-0.00314	418.255
2	10^{-6}	1.253226	-1.253184	626603.	-626602.	0.002385
2	10^{-3}	1.253725	-1.252684	627.102	-626.102	0.058962
2	10^{-1}	1.304221	-1.204180	6.78097	-5.78097	5.66722
2	1	1.849280	-0.849239	1.26727	-0.26727	58.1056
2	3	3.454620	-0.454579	1.01762	-0.01762	204.479
2	5	5.296522	-0.296480	1.00314	-0.00314	418.289
4	10^{-6}	1.253271	-1.253139	626603.	-626602.	0.007465
4	10^{-3}	1.253770	-1.252639	627.102	-626.102	0.064042
4	10^{-1}	1.304264	-1.204134	6.78096	-5.78096	5.67232
4	1	1.849308	-0.849177	1.26727	-0.26726	58.1129
4	3	3.454631	-0.454499	1.01762	-0.01761	204.510
4	5	5.296527	-0.296395	1.00314	-0.00314	418.3910

TABLE II. Direct image positions, their magnifications, and the time delay between secondary and primary images for the supermassive black hole M87* for different values of k and β in the weak deflection limit. All angles are in as, and the time delay is in units of hrs.

that for polymerized black hole with large values of k the outermost relativistic image can be distinguished from the pack of the higher order relativistic images. Similarly, the time delay Δt_{12} between the first two relativistic images is of the order of minutes for Sgr A* black hole, and of the order of hours for the M87* black hole and increases with k . Interestingly, for a given

source position, the time delay between the first and second relativistic images is larger than the time delay between the direct primary and secondary images, i.e., $\Delta t_{ps} < \Delta t_{12}$.

VI. POLYMERIZED BLACK HOLE SHADOWS UNDER DIFFERENT ACCRETION FLOW SCENARIO

The black hole's gravitationally lensed light rays, emanating from all the sources in the sky, construct the black hole image on the observer's screen. To mathematically generate this image it is practical to employ the relativistic backward ray-tracing method [107, 108]. In this method, we trace the rays backward in time from the observer's screen to the source using Eq. (26). Depending on the impact parameter $b \geq b_c$, the backtraced light rays from the observer can reach the source either directly or after completing any numbers of loops around the black hole. We assign some brightness to these light rays' directions. In contrary, light rays with $b < b_c$ get trapped in the black hole gravitational field and eventually spiral down to the black hole horizon and fall into it, accounting for the dark region on the observer's screen. This brightness depression on the observer's plane, enclosed by the bright circular ring at b_c , is known as the "black hole shadow" [17]. On the other hand, for light rays with $b \rightarrow b_c$, the number of winding n around the black hole rises exponentially such that for $b = b_c$, $n \rightarrow \infty$ and light rays converge to the critical curve. The path integral of such strongly lensed photons, arising from near-critical light rays, through the emission region diverge logarithmically, thus the image intensity, resulting in a bright ring [109, 110]. These lensed light rays appear within a narrow angular band, called the *photon ring*, at the shadow boundary on the observer's sky. The photon ring, as defined here, was called the "shadow apparent boundary" by Bardeen [17] and the "critical curve" by Gralla et al. [110]. While the photon rings or critical curve solely depends on the spacetime geometry, the shadow intensity distribution depends additionally on the details of the accretion models and emission processes. The possibilities of estimating the black hole parameters from the photon ring structure are discussed in detail in refs. [91, 111].

For an optically thin isotropic emitting region transparent to its own emission around a black hole, the image plane region $b < b_c$ would be dark while $b > b_c$ would be uniformly bright with a narrow bright ring with diverging intensity at $b \rightarrow b_c$. Interestingly enough, the shadow boundary location is independent of the inner radius at which the accreting gas stops radiating [53]. For the Schwarzschild black hole, the shadow boundary appears for $b_c = 3\sqrt{3}/2$. On the other hand, if the black hole is backlit by a distant planar and sufficiently large source screen with isotropic and uniform brightness, the black hole will cast a slightly larger shadow, extending

k	θ_{1p}	θ_{2p}	θ_{1s}	θ_{2s}	θ_∞	θ_{E1}	θ_{E2}	$\mu_1(10^{-18})$	$\mu_2(10^{-21})$	s	r_{mag}	$\Delta t_{12}(\text{min})$
0.	26.4287	26.33	-26.2969	-26.3298	26.3299	26.3628	26.3299	8.42316	15.7101	0.03295	535.159	11.4968
0.5	28.4899	28.3895	-28.3558	-28.3893	28.3893	28.4229	28.3894	9.24136	17.1757	0.03351	537.046	12.3961
1.	33.5802	33.4756	-33.4403	-33.4754	33.4754	33.5103	33.4755	11.3653	20.5861	0.03481	551.084	14.6169
1.5	40.151	40.0406	-40.0029	-40.0403	40.0404	40.077	40.0404	14.3922	24.9823	0.03661	575.094	17.4834
2.	47.3997	47.2819	-47.2414	-47.2816	47.2817	47.3205	47.2818	18.1517	30.157	0.03884	600.905	20.6453
2.5	54.986	54.8599	-54.8163	-54.8597	54.8597	54.9011	54.8598	22.5778	36.0834	0.04139	624.712	23.9542
3.	62.7585	62.6235	-62.5765	-62.6233	62.6233	62.6675	62.6234	27.6408	42.7511	0.04416	645.551	27.3441
3.5	70.6428	70.4985	-70.4479	-70.4982	70.4982	70.5453	70.4983	33.3251	50.1507	0.04717	663.498	30.7826
4.	78.5989	78.4449	-78.3907	-78.4446	78.4447	78.4948	78.4447	39.6217	58.2737	0.05015	678.923	34.2524

TABLE III. Relativistic image positions, their magnifications, relativistic Einstein rings, and strong lensing observables for the supermassive black holes Sgr A* for different values of k and $\beta = 1$ as. All angles are in μas .

k	θ_{1p}	θ_{2p}	θ_{1s}	θ_{2s}	θ_∞	θ_{E1}	θ_{E2}	$\mu_1(10^{-18})$	$\mu_2(10^{-21})$	s	r_{mag}	$\Delta t_{12}(\text{hrs})$
0.	19.8563	19.7822	-19.7573	-19.782	19.782	19.8068	19.7821	4.75466	8.86797	0.02475	535.159	289.648
0.5	21.4049	21.3295	-21.3041	-21.3293	21.3293	21.3545	21.3294	5.21651	9.69525	0.02517	537.046	312.304
1.	25.2293	25.1508	-25.1242	-25.1506	25.1506	25.1768	25.1507	6.41541	11.6203	0.02615	551.084	368.254
1.5	30.1661	30.0831	-30.0548	-30.0829	30.0829	30.1104	30.083	8.12403	14.1019	0.02750	575.094	440.473
2.	35.6121	35.5236	-35.4932	-35.5234	35.5235	35.5526	35.5235	10.2462	17.0228	0.02918	600.905	520.133
2.5	41.3118	41.2171	-41.1843	-41.2169	41.217	41.2481	41.217	12.7446	20.3681	0.03109	624.712	603.497
3.	47.1514	47.05	-47.0147	-47.0498	47.0498	47.083	47.0499	15.6025	24.1319	0.03318	645.551	688.902
3.5	53.075	52.9666	-52.9286	-52.9663	52.9664	53.0018	52.9664	18.8111	28.3088	0.03539	663.498	775.532
4.	59.0526	58.9368	-58.8961	-58.9366	58.9367	58.9743	58.9367	22.3654	32.894	0.03768	678.923	862.948

TABLE IV. Relativistic image positions, their magnifications, relativistic Einstein rings, and strong lensing observables for the supermassive black holes M87* for different values of k and $\beta = 1$ as. All angles are in μas .

out the critical curve; for Schwarzschild black hole, the shadow boundary appears at $b = 6.17/2$ still with a photon sphere at $b = b_c = 3\sqrt{3}/2$. This additional dark region $6.17/2 \leq b \leq 3\sqrt{3}/2$ accounts for the light rays having deflection angle $\pi/2 < \alpha_D < 3\pi/2$, whereas the main bright region $b > 6.17/2$ corresponds to the light having deflection angle smaller than the $\pi/2$. Close to the critical curve, a series of converging and demagnified photon rings exist that account for the multiple winding around the black hole [110].

Whereas for planar and optically thin accretion disks, whose emission is confined to the equatorial plane, the central brightness depression extends simply to the lensed position of the inner edge of the disk, and is bounded by a bright photon ring with diverging intensity. However, in contrast to the spherical accretion model, this photon ring can typically be decomposed into a series of infinitely many concentric discrete photon rings, which are organized self-similarly and depend on the number of loops executed around the black holes. However, only a few subrings can be resolved as the higher-order rings are highly closely packed and demagnified [52, 112]. In particular, for the accretion disk extending up to the black hole's event horizon, the shadow boundary does not coincide with the critical curve but rather is restricted to a much smaller area—*an inner shadow*—whose edge lies near the direct lensed image of the equatorial horizon [109, 112]; for Schwarzschild black hole ($x_+ = 1$) it appears at $x = 1.45$. The inner shadow forms by the light

rays, which fall into a black hole without crossing the equatorial plane once, i.e., $n < 1/4$. Furthermore, these models still feature a photon ring. For these models, the darkest region in the observed image will correspond to the inner shadow. However, due to the increasingly large gravitational redshift at the event horizon, the image brightness falls sharply around the inner shadow edge. In contrast, the spherical accretion models do not give rise to the inner shadow. Due to this reason, the EHT images released thus far do not resolve the inner shadow of M87, as they also lack the requisite resolution.

The black hole shadow features depend not only on the spacetime geometry but also on the surrounding accretion details. This section analyzes the effect of the polymerized black hole accretion flow on the shadow images by considering three different scenarios namely, a black hole under the static spherical accretion, a black hole surrounded by an optically thin accretion disk, and radially infalling accretion onto the black hole.

A. Static Spherical Accretion Flow

We begin by considering that the polymerized black hole is surrounded by an optically thin, spherically symmetric, and isotropic radiating gas, which is at rest and extends up to the horizon. In the rest-frame of the gas, the emitted specific intensity is \mathcal{I}_ν^{em} at photon frequency ν_{em} . We consider an observer at a far distance

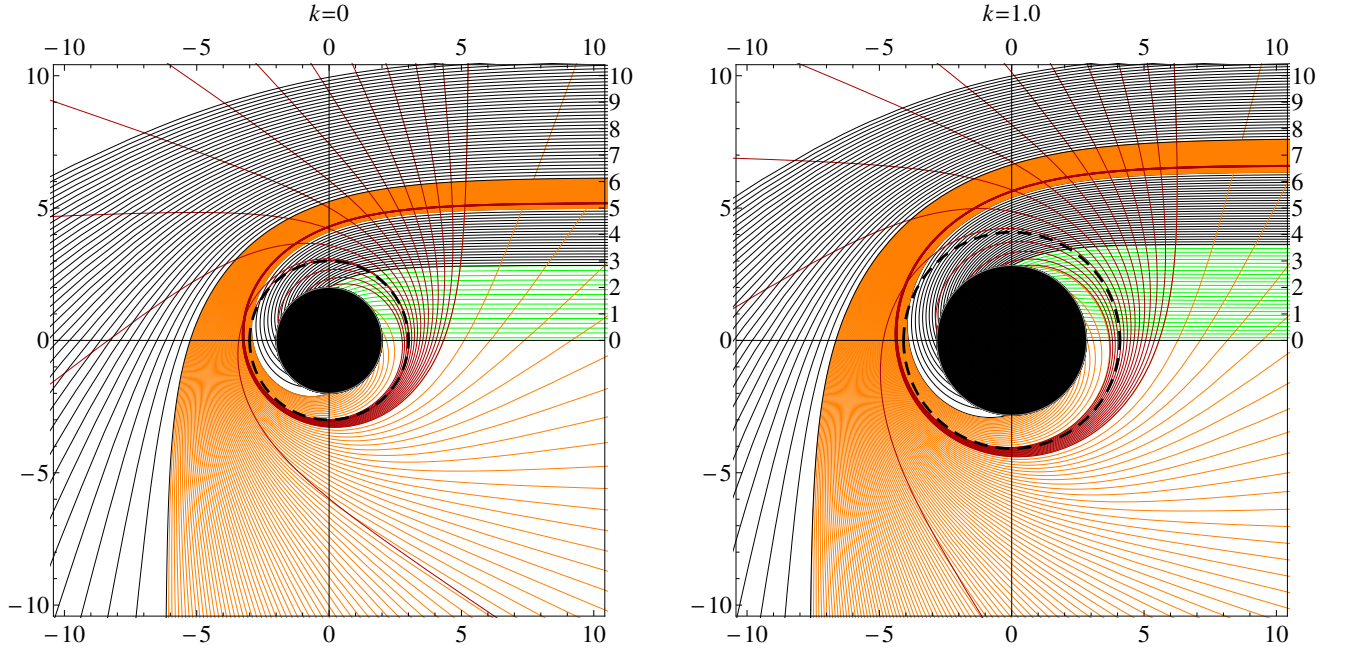


FIG. 9. Photon geodesics behavior as a function of impact parameter u . Color classified geodesics based on their number of equatorial plane crossing $n = \frac{\phi}{2\pi}$ (see text for details). The black hole is shown as a solid disk and the critical curve as a closed black dashed circle.

from the black hole $x_{obs} \rightarrow \infty$; the observed specific intensity \mathcal{I}_ν^{obs} at the photon frequency ν_{obs} can be obtained by integrating the emissivity along the photon path γ as follows [113, 114]

$$\mathcal{I}_\nu^{obs} = \int_\gamma z^3 j(\nu_e) dl, \quad (77)$$

where the redshift factor z quantifies the change in a photon's frequency as it traverses through spacetime from the point of emission x_{emit} to the point of detection x_{obs} defined as

$$z = \frac{\nu_{obs}}{\nu_e} = A(x)^{1/2}, \quad (78)$$

and $j(\nu_{em})$ is the emissivity per-unit volume (specific emissivity) measured in the rest-frame of the gas. Here, we assume that the emission is monochromatic and the emission radial profile is $1/x^2$, that is [68, 114]

$$j(\nu_{em}) = \frac{\delta(\nu_{em} - \nu_{obs})}{x^2}, \quad (79)$$

where δ is the Dirac delta function. The infinitesimal proper length along the photon path is

$$dl = \sqrt{B(x) dx^2 + C(x) d\phi^2} \quad (80)$$

$$= \sqrt{\frac{B(x)C(x)}{C(x) - A(x)b^2}} dx. \quad (81)$$

Therefore, the observed total photon intensity can be obtained by integrating Eq. (77) for all observed

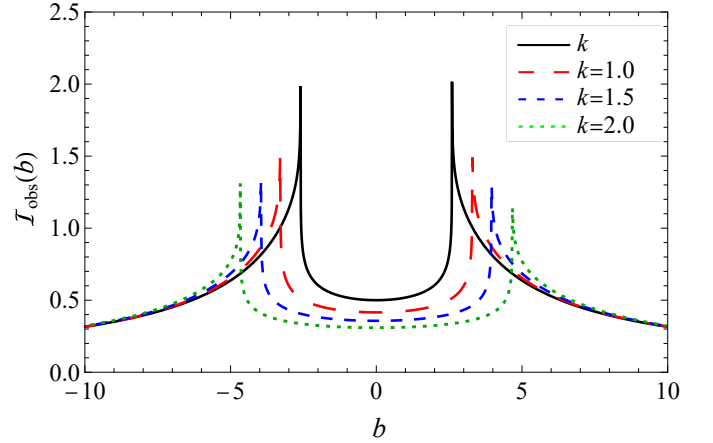


FIG. 10. The observed total intensity map for the static spherically symmetric accretion around polymerized black hole as a function of impact parameter b . For comparison the intensity distribution for the Schwarzschild black hole is also shown with black line.

frequencies, and it takes the following form [53, 114]

$$\mathcal{I}_{obs} = \int_\gamma \frac{A(x)^{3/2}}{x^2} \sqrt{\frac{B(x)C(x)}{C(x) - A(x)b^2}} dx. \quad (82)$$

The γ in Eq. (82) signifies that the integral has to be evaluated along the path of the photon. It is interesting to note that, unlike the photon circular orbit radius and the shadow size, which are determined only by $A(x)$, the

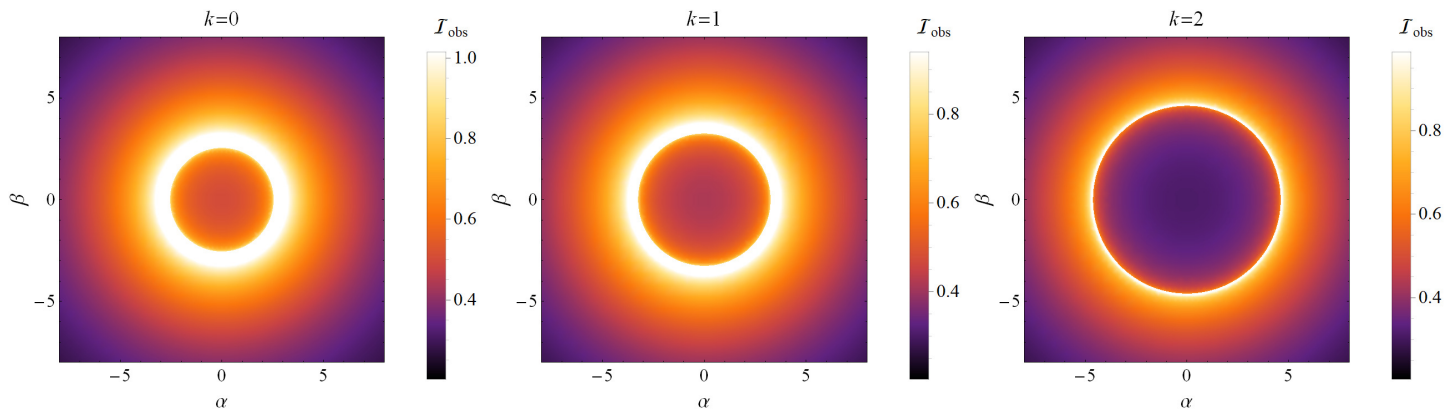


FIG. 11. Polymerized black hole shadows with the static spherical accretion for the different values of k as seen by a distant observer.

intensity distribution additionally depends on the metric function $B(x)$. Because the gas is uniformly distributed, and optically thin, emitted light can propagate in all directions and travel arbitrarily large distances without being absorbed or scattered. For the black hole image, however, we only track light rays that reach the observer. We employ a numerical technique – backward ray-tracing technique. For $b \leq b_c$, the light rays are backtraced from the observer to the horizon, whereas for $b > b_c$, light rays are backtraced from the observer to some turning point and then to the emitter position. Using Eq. (82), we calculated the observed total photon intensity and showed it in Fig. 10. With the decreasing impact parameter ($b > b_c$), the \mathcal{I}_{obs} increases rapidly and reaches a peak at $b = b_c$ and then sharply falls to a lower value. This expected intensity depression at the center is the black hole shadow signature. These shadows are shown in Fig. 11, where we present the two-dimensional intensity map in celestial coordinates (α, β) . Different colors correspond to different values of the observed intensity, and we use one color function for all shadow plots, where the greater (smaller) intensity means the brighter (darker) color. The salient feature of the shadow is that the intensity is circularly symmetric and it possesses a circular bright ring at $b = b_c$ with the strongest luminosity, which in principle is the position of the photon sphere with diverging intensity. However, due to the limitation of calculation accuracy and the logarithmic form of the divergence (integrand in the Eq. (82) diverges for the limit $x \rightarrow x_c$), the calculated intensity will never reach infinity (cf. Fig. 10). It is worth noting here that the peak is not at the position of the inner edge of the emitting gas, $x = 1$, rather it is at the photon ring b_c , corresponding to the lensed image of the photon orbit. From Fig. 11, we can directly compare the intensity magnitude inside and outside the photon ring, and it is clear that the inner region of the photon ring is not completely dark with zero intensity, such as would be observed if the radiating gas were entirely behind the black hole. The non-zero intensity

at $b = 0$ arises because the radiating gas is also present along the lines of sight that intersect the surface of the black hole, and tiny fraction of that radiation inside the photon ring can always escape to an observer at infinity. In particular, for $x > x_c$, the solid angle of the escaping rays is $2\pi(1 + \cos\theta)$ and for $x < x_c$ the solid angle of escaping rays is $2\pi(1 - \cos\theta)$ with θ as

$$\theta = \arcsin\left(\frac{x_c^{3/2}}{x}\sqrt{A(x)}\right). \quad (83)$$

The net luminosity observed at infinity

$$L_\infty = \int_{x_+}^{x_c} 4\pi x^2 j(\nu_e) 2\pi(1 - \cos\theta) dx \quad (84)$$

$$+ \int_{x_c}^{\infty} 4\pi x^2 j(\nu_e) 2\pi(1 - \cos\theta) dx. \quad (85)$$

While the peak value of intensity at the photon ring decreases with k , the luminosity depression within the shadow increases and the shadow size grows with k (cf. Fig. 10). Figure 11 implies that the polymerized black holes have larger shadows with darker interiors than Schwarzschild black holes. In addition, polymerized black holes have a smaller brightness near the photon ring than those of Schwarzschild black holes. The fraction intensity depression f_c , defined as the ratio of intensity at the center $b = 0$ and just outside the photon ring $b = b_c + 0.1$, for $k = 0, 1$ and 2 , respectively, is $f_c = 0.30, 0.288$, and 0.272 . f_c decreases with k and this can be seen in Fig. 11.

B. Accretion Disk Flow

In our next example, we analyze a simple case of the emission from an optically and geometrically thin disk-shaped accretion flow at the equatorial plane outside the polymerized black hole. We further assume that the disk emits isotropically in the rest frame of the observer located at a far distance from the black hole in the north

pole direction. The light trajectories are shown in Fig. 9. We conveniently orient our setup, such that the vertical black line represents the black hole's accretion disk at $\theta = \pi/2$ and the observer is on the right hand side of the black hole ($\theta = 0$) that is shown as the black disk. In order to implement our numerical simulation of the black hole shadow, we first summarize the important light trajectories.

1. Direct emission, lensed ring and photon ring

In earlier subsections, we classified the light geodesics based on their impact parameter, whether they plunge into the black hole ($b \leq b_c$) or scatter and escape to the observer ($b > b_c$). Following Gralla *et al.* [110], we further characterized light ray trajectories by the number of the crossing of the black hole's equatorial plane $n = \frac{\phi}{2\pi}$ outside the horizon. Here, ϕ is the total shift in the azimuthal angle for a given light ray trajectory outside the horizon.

- **Direct Rays Type-1:** Rays crossing equatorial plane only once ($\frac{1}{2} \leq n < \frac{3}{4}$) with $\pi \leq \phi < \frac{3\pi}{2}$. While back-tracing these rays meet the background source ($b > b_c$), and make dominant contribution to the black hole image. These rays are deflected by angle less than 90° . Photons not being deflected at all by the black hole ($b \gg b_c$) follow straight line motion and correspond to $n = \frac{1}{2}$. These rays are shown as black curves outside the critical curve in Fig. 9.
- **Direct Rays Type-2:** Rays crossing equatorial plane only once ($\frac{1}{2} \leq n < \frac{3}{4}$) with $\pi \leq \phi < \frac{3\pi}{2}$. The salient feature of these rays is that while back-tracing these rays *do not* meet the background source but rather fall into the black hole ($b < b_c$), this makes them different from the direct rays type-1, shown as black curves inside the critical curve in Fig. 9. These rays are also deflected by an angle less than 90° .
- **Lensing Ring:** Rays crossing the equatorial plane twice ($\frac{3}{4} \leq n < \frac{5}{4}$) with $\frac{3\pi}{2} \leq \phi < \frac{5\pi}{2}$. While these light rays with $b > b_c$ connect the observer to the source on the same side, those with $b < b_c$ fall into the black hole. These rays are shown as orange curves in Fig. 9.
- **Photon Ring:** Rays crossing the equatorial plane three or more times ($n > \frac{5}{4}$) with $\phi > \frac{5\pi}{2}$ and $b \gtrsim b_c$. These light rays follow multiple winding around the black hole. These rays are shown as red curves in Fig. 9.
- **Critical Curve:** Rays following infinite winding around the black hole $n \rightarrow \infty$ with $b = b_c$. Higher-order photon rings rapidly converge to the

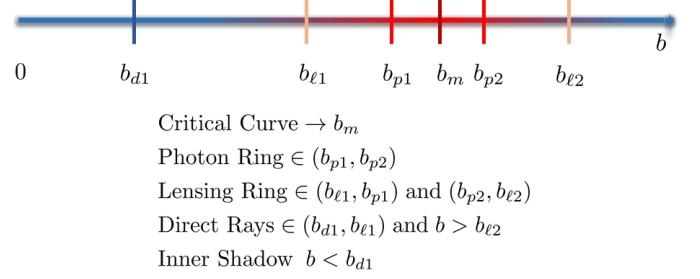


FIG. 12. Various light ray trajectories classified by their impact parameter.

critical curve shown as a black dashed circle in Fig. 9.

- **Inner Shadow:** Rays that do not cross the equatorial plane before intersecting the event horizon ($b < b_c$). These rays are shown as green curves inside the critical curve in Fig. 9.

The impact parameter window allowing a certain number of half-orbits $n > \frac{5}{4}$ is quickly diminished and corresponding rings are highly demagnified [40]. Each winding of light rays around a black hole constructs a new closed photon ring that is indexed by the equatorial plane crossing number. For instance, light rays with $\frac{5\pi}{2} + 2m\pi < \phi \leq \frac{7\pi}{2} + 2m\pi$ with m as an integer, construct a m th order photon ring around the black hole. These higher-order photon rings asymptote to the critical curve. The contribution of these higher-order photon rings to the black hole's optical appearance is exponentially suppressed as compared to that of the direct emission. Interestingly, light rays with $b < b_c$ will also perform a number of half orbits on their trip down to the event horizon. These orbits are indeed crucial for the accretion disk models where the inner edge of the disk is allowed to extend inside the outer photon sphere.

With this classification, as summarized in Fig. 12, we first back-trace the light rays with $b > b_c$ from the observer at x_{obs} till the distance of closest approach x_0 and then to the emitter. While for the light ray with $b < b_c$, the tracing ends as the ray reaches the horizon at a finite value of ϕ

$$b > b_c, \quad n = \frac{1}{2\pi} \left(\int_{x_{emit}}^{x_0} \frac{d\phi}{dx} dx + \int_{x_0}^{x_{obs}} \frac{d\phi}{dx} dx \right), \quad (86)$$

$$b < b_c, \quad n = \frac{1}{2\pi} \int_{x_+}^{x_{obs}} \frac{d\phi}{dx} dx. \quad (87)$$

We numerically computed the impact parameter ranges for the lensing ring, photon ring, and direct emission and summarized them in the table. V. Figure 13 shows the total number of orbits as a function of the b and different values of k . With the increase of the value of k , the range

Classes	$k = 0$	$k = 0.5$	$k = 1.0$
Direct Rays Type-1	$u \notin (5.0152, 6.1669)$ $u > 6.1669$	$u \notin (5.40767, 6.58743)$ $u > 6.58743$	$u \notin (6.3787, 7.6383)$ $u > 7.6383$
Direct Rays Type-2	$2.8477 < u < 5.0152$	$3.071 < u < 5.40761$	$3.626 < u < 6.3787$
Lensing Ring	$u \in (5.0152, 5.18781)$ $u \in (5.22793, 6.1669)$	$u \in (5.40767, 5.59362)$ $u \in (5.63493, 6.58743)$	$u \in (6.3787, 6.59598)$ $u \in (6.640098, 7.6383)$
Photon Ring	$u \in (5.18781, 5.22793)$	$u \in (5.59362, 5.63493)$	$u \in (6.59598, 6.640098)$
Critical Curve	$u \equiv u_c = 5.1962$	$u \equiv u_c = 5.60259$	$u \equiv u_c = 6.60632$
Inner Shadow	$u < 2.8477$	$u < 3.071$	$u < 3.626$

TABLE V. In this table we depict the various lensing features for different values of k . The impact parameter for the direct, lensing, photon rings and inner shadows are shown and compared with the Schwarzschild black hole values (see Sec. III for details).

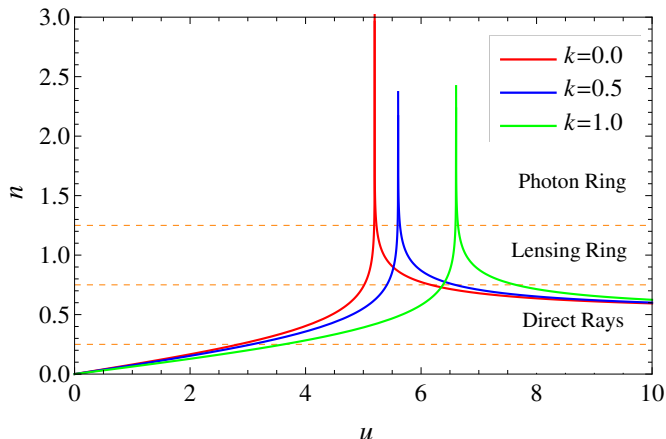


FIG. 13. Number of half-orbits n as a function of impact parameter b for different values of k . Three orange colored dashed horizontal lines are for photon ring, lensed, and direct emission regions, respectively, with $n = 5/4, 3/4, 1/4$ (from top to bottom).

of b occupied by the lensing ring and the photon ring becomes large and the corresponding impact parameters also increase. This implies that the polymerized black holes have thicker lensing and photon rings compared to those for the Schwarzschild black hole. Using the strong lensing deflection angle Eq. (56), one can calculate the impact parameter b corresponding to light rays with number of crossings of the equatorial plane n ,

$$b = b_c \left(1 + e^{-\frac{(2n-1)\pi - \bar{q}}{\bar{p}}} \right), \quad (88)$$

which implies that as $n \rightarrow \infty$, $b \rightarrow b_c$.

2. Shadow images

We are presuming that the light is only emitted from the accretion disk and that other effects, such as light absorption or reflection, are insignificant. The observed photon specific intensity at frequency ν_{obs} is $\mathcal{I}_\nu^{obs} = z^3 \mathcal{I}_\nu^{em}$, which can be integrated for the full frequency

spectrum to get the total observed photon intensity

$$\mathcal{I}_{obs} = z^4 \mathcal{I}_{em}, \quad (89)$$

where z is the redshift factor (78). As shown in Fig. 9, for the direct emission (black trajectories), the backtraced light from the observer falls on the front side of the accretion disk, whereas for the lensed emission (orange trajectories), the light bent around the black hole crosses the equatorial plane once and falls on the back side of the accretion disk. The light is even directed to make a complete loop around black hole and return to the front side of the accretion disk for the photon ring emission (red trajectories). Nevertheless, as earlier discussed, depending on the impact parameter b , light rays pass through the accretion disk for $n(b)$ times. With each crossing the light rays pick up a certain luminosity and transmit it to the observer. Hence, the total observed intensity at the observer's screen is the sum of the intensity from each intersection

$$\mathcal{I}_{obs} = \sum_n A(x)^2 \mathcal{I}_{em}|_{x=x_n(b)}, \quad (90)$$

where $x_n(b)$, known as the transfer function, is the radial position of the n_{th} crossing of the accretion disk. In this case, careful consideration is necessary to find higher-order $x_n(b)$ as these are highly sensitive to b . Gralla *et al.* [110] identified the slope dx/db as the demagnification factor of the corresponding light rays. For the purpose of this work, $n = 1; 2; 3$ denotes the direct, lensed and photon ring emission, neglecting additional intersections with the disk since they will presumably contribute much less to the total luminosity [40]. We calculated $x_n(b)$ and showed their behavior with b in Fig. 14. The first three transfer function are shown with the black, orange and red lines. The black line, $x_1(b)$, accounting for the first transfer function and direct image of the disk, has a slope approximately equal to 1, therefore, it makes the major contribution to the disk image intensity. Orange $x_2(b)$ and red $x_3(b)$ lines have slope much larger than 1, and accounts for the demagnified lensed images of the back side and front side of the disk, respectively. Here, we consider a toy accretion disk model, previously investigated by [115–119]. The inner edge of the accretion

disk matches with the innermost stable circular orbit (ISCO) location and the emission exists only for $x > x_{isco}$

$$\mathcal{I}_{em}(x) = \begin{cases} \left(\frac{1}{x-(x_{isco}-1)}\right)^2 & x \geq x_{isco} \\ 0 & x < x_{isco}. \end{cases} \quad (91)$$

The black hole's ISCO radius can be determined by $V_{\text{eff}} = E^2, V'_{\text{eff}} = 0$, and $V''_{\text{eff}} = 0$. Using Eqs. (90)-(91), the total emitted intensity $\mathcal{I}_{em}(x)$ as a function of x , the total observed intensity $\mathcal{I}_{obs}(b)$ as a function of b , and the two-dimensional image in celestial coordinates are plotted in the Fig. 15. The observed intensity plot in Fig. 15 allows for a clear view of the three intensity peaks of light rings associated to direct, lensed, and photon ring emissions. For $k = 0$, the emission function peaks at the ISCO, $x = 3$, while, the observed direct emission peaks at $b = 3.49$ and has an additional lensed image emission at $2.775 \leq b \leq 3.025$ and a photon ring at $b = 2.628$. Similarly, for $k = 1.0$, the emission function peaks at the ISCO, $x = 4.249$, while, the observed direct emission peaks at $b = 4.759$ and has an addition lensed image emission at $3.492 \leq b \leq 3.734$ and a photon ring at $b = 3.321$. The contribution from the photon rings and the lensing rings emission is small compared to the direct emission. Because the accretion disk is orthogonal to the line of sight of the observer to the black hole, the lensed image of the disk is circularly symmetric as shown in the right panel of Fig. 15. The outermost boundary of the dark region and the inner bright ring, respectively, are due to the direct emission coming from disk and the lensed emission forming the secondary images of disk. Even though the direct emission dominates the total luminosity, a bright extended lump of radiation enclosing a thinner and dimmer ring and an even thinner photon ring (which is barely visible at naked eye) are the prominent features in the image. As a result, when compared to the spherical model, the geometrically thin disks model has different shadow features. An interesting and important analytical study of higher-order ring images of accretion disk around black hole is presented in Refs. [120, 121].

C. Infalling Spherical Accretion Flow

Let us consider a more realistic scenario, where the surrounding optically-thin radiating gas undergoes radially free-fall motion onto the black hole but emitting isotropically. The observed specific intensity for the photon frequency ν_{obs} at the point (α, β) on the observer's screen is still defined by Eq. (77). However, because of the relative motion between the infalling gas and the static observer, the redshift factor is different from the static accretion case. Indeed, the redshift factor is evaluated as [53, 114]

$$z = \frac{p_\rho u_\rho^p}{p_\sigma u_\sigma^e}. \quad (92)$$

Here, $p^\mu = \dot{x}_\mu$ is the photon four-momentum, and $u_\rho^\mu = (1, 0, 0, 0)$ is the static observer's four-velocity at far distance from the black hole, and u_e^μ is the four-velocity of the accreting gas emitting the radiation under radial free fall, which is

$$u_e^\mu = \left(\frac{1}{A(x)}, -\sqrt{\frac{1-A(x)}{A(x)B(x)}}, 0, 0 \right), \quad (93)$$

such that $u_e^\mu u_{e\mu} = -1$. Hence, the redshift factor of the infalling accretion is calculated as

$$z = \left(\frac{1}{A(x)} - \frac{p_r}{p_t} \sqrt{\frac{1-A(x)}{A(x)B(x)}} \right)^{-1}, \quad (94)$$

which, as expected, is a function of x and b . Whereas the photon four-momentum satisfies $p_\mu p^\mu = 0$ and

$$p_r = \pm p_t \sqrt{\frac{B(x)}{A(x)} - \frac{b^2 B(x)}{C(x)}}, \quad (95)$$

where, the sign $+$ ($-$) corresponds to the photon moving toward (moving away from) black hole. The infinitesimal proper length as measured in the rest-frame of the accreting gas can be defined as [85]

$$dl_{prop} = -p_\mu u_e^\mu d\lambda = \frac{p_t}{z p^x} dx, \quad (96)$$

and not $\frac{p_t}{z p^x} dx$ as wrongly reported in many papers. Integrating the observed specific intensity over all the observed photon frequencies, we get the total observed photon intensity [53, 85, 114]

$$\mathcal{I}_{obs} \propto - \int_\gamma \frac{z^4}{x^2} dl_{prop} \propto - \int_\gamma \frac{z^3 p_t}{x^2 p^x} dx. \quad (97)$$

Because the observer is on one side of the black hole, for the radiating matter at the opposite side of the black hole, the infalling matter and the emitted light rays that reach the observer have motion in the same direction. In contrast, for the radiating matter on the same side of the black hole, the emitted light rays move against the infalling matter direction to reach the observer. As a result, both light rays experience distinct redshifts– Doppler beaming. For $b \leq b_c$, all light rays are backtraced from the observer to the horizon and are highly redshifted and contribute to the dark shadow interior. However, light rays with $b \geq b_c$, are redshifted from the observer x_{obs} to the turning point x_{tp} and blueshifted from the turning point x_{tp} to the emitter position x_{emit} . The blueshifted photon illuminates the black hole image. The observed intensity takes the form

$$\mathcal{I}_{obs}(\nu_o) \propto - \int_{x_{emit}}^{x_{tp}} \frac{z_-^3 p_t}{x^2 |p^x|} dx + \int_{x_{tp}}^{x_{obs}} \frac{z_+^3 p_t}{x^2 |p^x|} dx, \quad (98)$$

where z_+ and z_- , respectively, are the redshift and blueshift of the light rays.

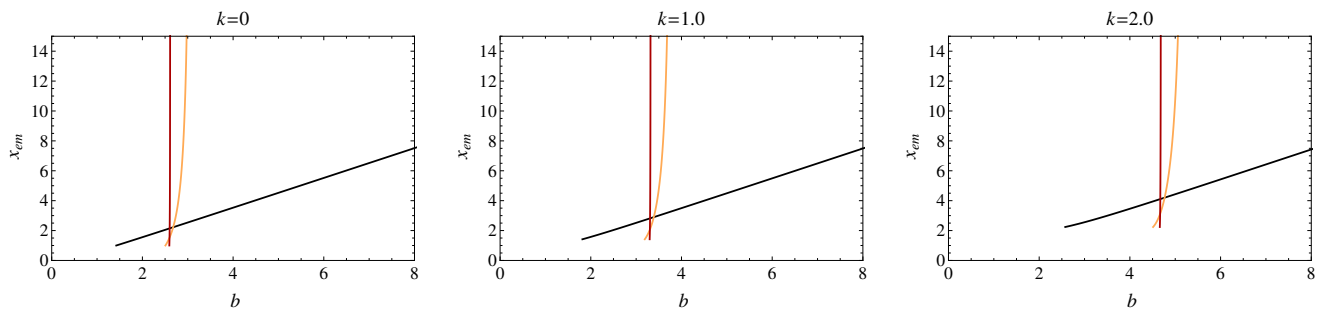


FIG. 14. First, second, and third transfer functions are shown with varying impact parameter b , respectively, with black, orange, and red colors lines. They also correspond to the direct, lensing rings and photon rings. The slope of each curve is interpreted as the demagnification factor of the corresponding emission (see text for details).

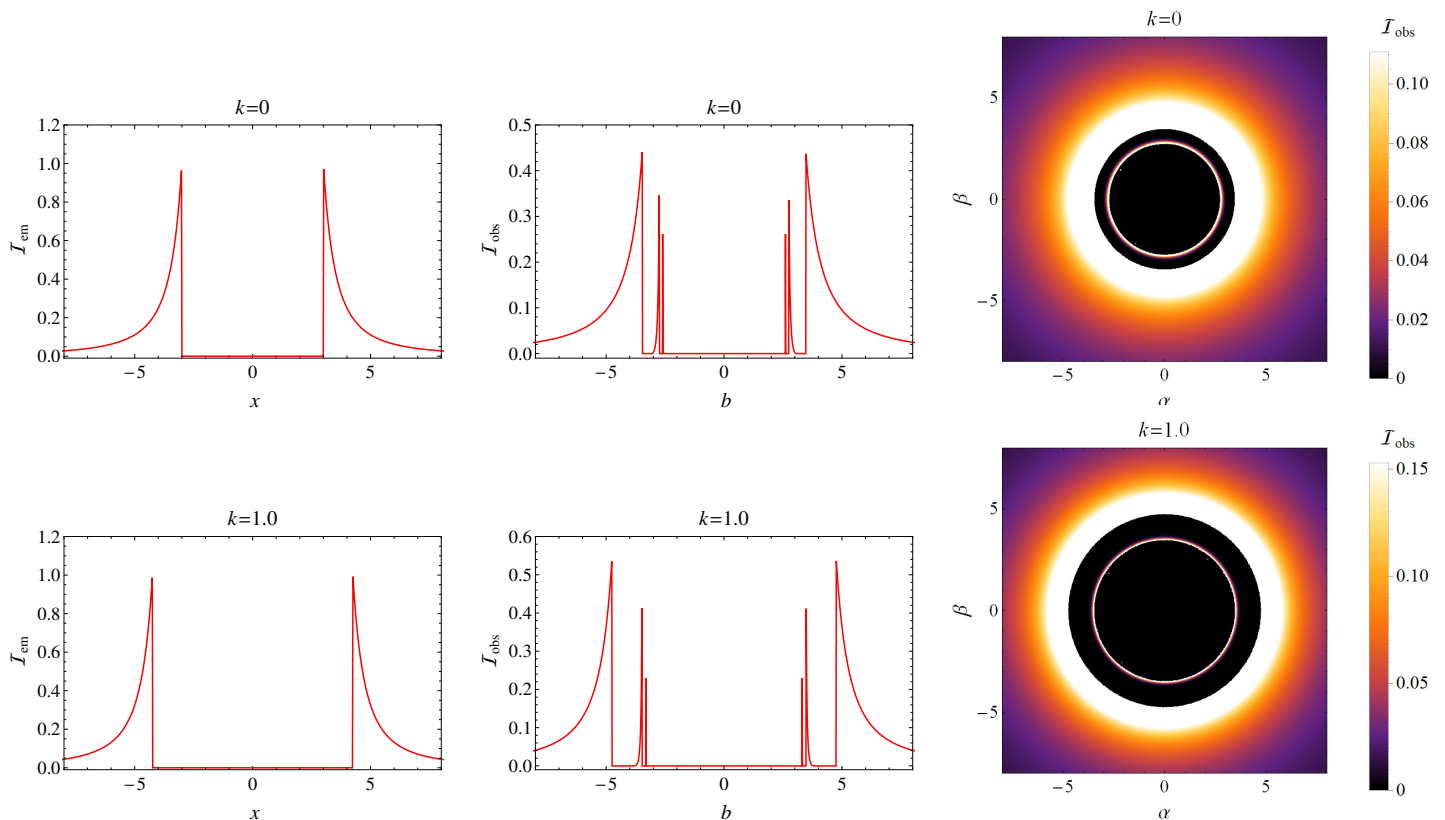


FIG. 15. Total emission intensity as a function of x (left), the observed total intensity as a function the b (middle), and the shadow images (right) for the polymerized black hole surrounded by an accretion disk.

We calculated and depicted the observed intensity as a function of b for different values of k in Fig. 16. The two-dimensional images of the shadow with an infalling spherical accretion seen by a distant observer are shown in Fig. 17. The intensity distribution qualitatively resembles that for the static accretion model, with intensity rising sharply with decreasing b , reaching a peak at $b = b_c$, and then dropping to significantly lower values inside the peak. However, there are important differences. Even while the measured intensity's peak value at the photon ring decreases with k , it is substantially smaller than that for the static

model. The central region inside the photon ring has a severely reduced brightness. In fact, it is clear that the shadow interior with infalling accretion in Fig. 17 is darker than the corresponding region for the static accretion as shown in Fig. 11. The clear contrast between these static and infalling models is due to the Doppler effect, which is more noticeable near the black hole's event horizon. In addition, the photon orbit radii and the shadow radii remain unchanged with accretion model. This confirms that the shadow is an inherent property of spacetime and that the behavior of the accretion flow surrounding the black hole only effects the intensity

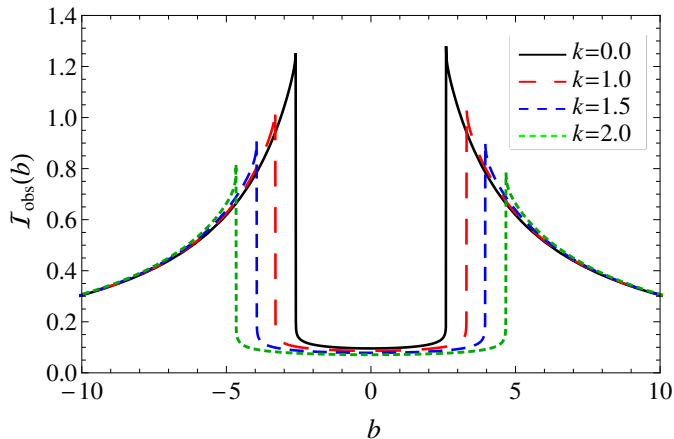


FIG. 16. The observed intensity map for the radially infalling accretion around a polymerized black hole as a function of the impact parameter b . For comparison, the intensity distribution for the Schwarzschild black hole is also shown with a black line.

of the images. The most striking feature of these images is the very high sensitivity of the shadow size to the value of k . Such a large difference in the image size would easily be detected with current observational techniques. Shaikh *et al.* [85, 122], and Joshi *et al.* [123] have reported that some naked singularities may also show black hole like shadow features. An interesting comparison between Schwarzschild black hole shadows produced under spherical and optically thin accretion in Newtonian model, static accretion model, and radially accretion model is presented in [53]. The bottom line of the discussion above is that under spherical accretion polymerized black holes cast larger shadows with lower brightness contrast compared to that for the Schwarzschild black hole. The fraction intensity depression f_c , for $k = 0, 1$ and 2 , respectively, is $f_c = 0.077, 0.0844$, and 0.092 .

VII. CONSTRAINTS FROM THE EHT 2017 OBSERVATIONS

The structure of Sgr A* and M87* black holes gets completely washed out by interstellar scattering at cm and higher wavelengths. However, at the mm wavelength, it is possible to image the emission region of these supermassive black holes due to three favorable reasons: (i) neglecting interstellar scattering, (ii) better angular resolution, and (iii) the compact synchrotron emitting region becomes optically thin. Indeed, the advent of the EHT, a global very long baseline interferometry (VLBI) network of radio telescopes observing at a frequency of 230GHz, made it possible to make horizon-scale observations of the supermassive black holes at the centers of galaxies. Recently, EHT

unraveled the first shadow images of Sgr A* black hole [18–20], which complement the observed shadow of M87* black hole in 2019 [21–24]. The observed shadows of both the Sgr A* and M87* black holes have a common feature that show a bright ring of emission surrounding a brightness depression. The size of the emission ring has been measured with unprecedented accuracy. The observed shadows of the Sgr A* and the M87* black holes have been extensively used to test alternative to Kerr black hole [32, 124–133]. Because the black hole spin introduces minor corrections to the size of the shadow [24, 91, 124], we can safely focus on nonspinning spacetimes. In addition, the spherically symmetric black hole shadow size only involves the information of the tt -component of the metric. Fortunately, the polymerized parameter k appears in the tt -component of metric (1), and as we have seen in the earlier sections, the shadow size strongly depends on the value of the k . Our goal in this section is to compare the LQG-motivated polymerized black hole shadows with those observed for the Sgr A* and M87* and to use the EHT bounds to place constraints on the polymerized black hole.

A. Constraints from M87* shadow

The observed emission ring angular diameter of the M87* black hole is $\theta_d = (42 \pm 3)\mu\text{as}$, with the estimated mass $M = (6.5 \pm 0.9) \times 10^9 M_\odot$ and distance $D_{LS} = 16.8 \pm 0.7$ Mpc. It is important to note that the EHT observation of the M87* black hole measured the size of the bright ring of emission and not the shadow angular diameter, therefore, we calibrated the emission ring diameter to that of the shadow by 10% [18]. Using this information, we calculate the shadow diameter for the M87* black hole in units of black hole mass

$$d_{M87}^I = \frac{D_{LS}\theta_d}{M} \approx 11.03 \pm 1.788, \quad (99)$$

with 10% offset for shadow size

$$d_{M87}^{II} \approx 9.92 \pm 1.609. \quad (100)$$

We consider the polymerized black hole model for the M87* and calculate the shadow diameter d_{M87} and depict it in Fig. 18. The blue and red lines in Fig. 18, account for the uncertainties in the estimated mass and distance of the M87* black hole. We then apply the EHT-imposed bound for the M87* shadow size to the polymerized black hole shadows. Because the polymerized black hole shadow size increases with k , the lower bound of M87* shadow angular diameter is mostly irrelevant for our purpose of constraining polymerized black hole parameters. With $M = 6.5 \times 10^9 M_\odot$ and $D_{LS} = 16.8$ Mpc, polymerized black hole with $k \leq 0.60$ satisfies the 1σ bound for M87* shadow size (black line in Fig. 18). Whereas, accounting for the uncertainties in M87* mass and distance, M87* shadow diameter within the 1σ and

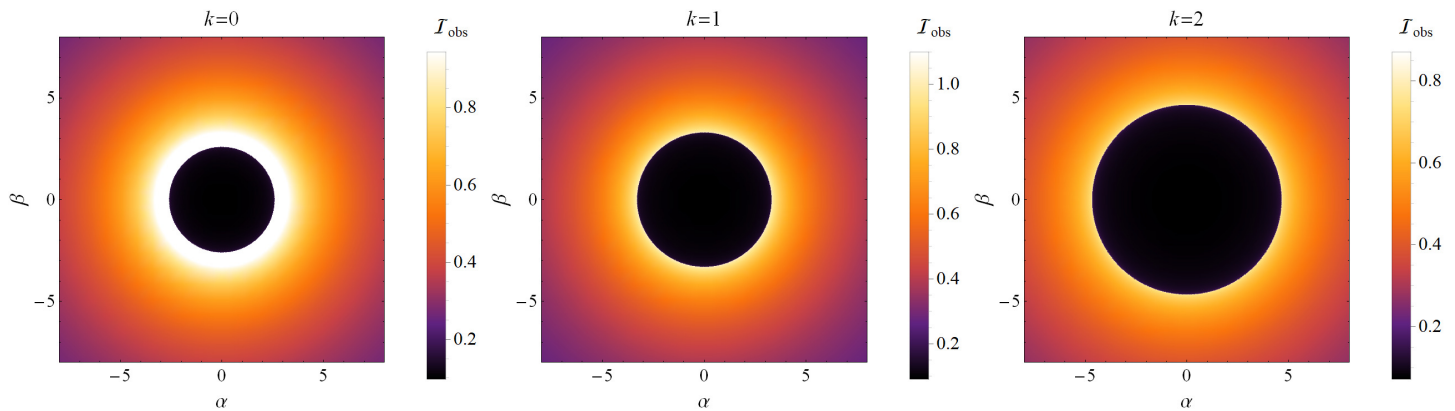


FIG. 17. Polymerized black hole shadows with the radially infalling spherical accretion for the different values of k as seen by a distant observer.

2σ confidence intervals, respectively, places constraints on $k \leq 1.06$ and $k \leq 1.42$ (red line in Fig. 18).

B. Constraints from Sgr A* shadow

Sgr A* black hole shadow images have advantages to test the nature of astrophysical black hole (i) Sgr A* black hole mass bridges the gap between the stellar black holes observed by the LIGO and the M87* black hole, and thus probes a significantly distinct curvature scale (10^6 order of higher curvature than the M87*) (ii) independent prior estimates for mass to distance ratio are used for Sgr A*. Most prominently, for the Sgr A* black hole, the EHT not only measured the emission ring angular diameter $\theta_d = (51.8 \pm 2.3)\mu\text{as}$ but also estimated the shadow diameter $\theta_{sh} = (48.7 \pm 7)\mu\text{as}$ with the priors $M = 4.0^{+1.1}_{-0.6} \times 10^6 M_\odot$ and $D_{LS} = 8.15 \pm 0.15$ kpc [21]. For instance, EHT used three independent imaging algorithms, namely, `eht-imaging`, SIMLI, DIFMAP, to determine the Sgr A* shadow morphology. The most likely averaged measured value of the shadow angular diameter from these three algorithms is in the range $\theta_{sh} \in (46.9 - 50)\mu\text{as}$, and the 1σ credible interval is $41.7 - 55.6\mu\text{as}$ [21, 22]. The shadow diameter reads as

$$d_{Sgr} = \frac{D_{LS}\theta_{sh}}{M} \in (9.6931, 10.3338), \quad (101)$$

and the 1σ credible interval

$$d_{Sgr} \in (8.61839, 11.4912). \quad (102)$$

Furthermore, EHT used the observable δ to quantify deviation between the inferred shadow diameter and that of a Schwarzschild black hole as follows [21, 22]

$$\delta = \frac{\theta_{sh}}{\theta_{sh,Sch}} - 1. \quad (103)$$

EHT used the two separate priors for the Sgr A* angular size from the Keck and Very Large Telescope

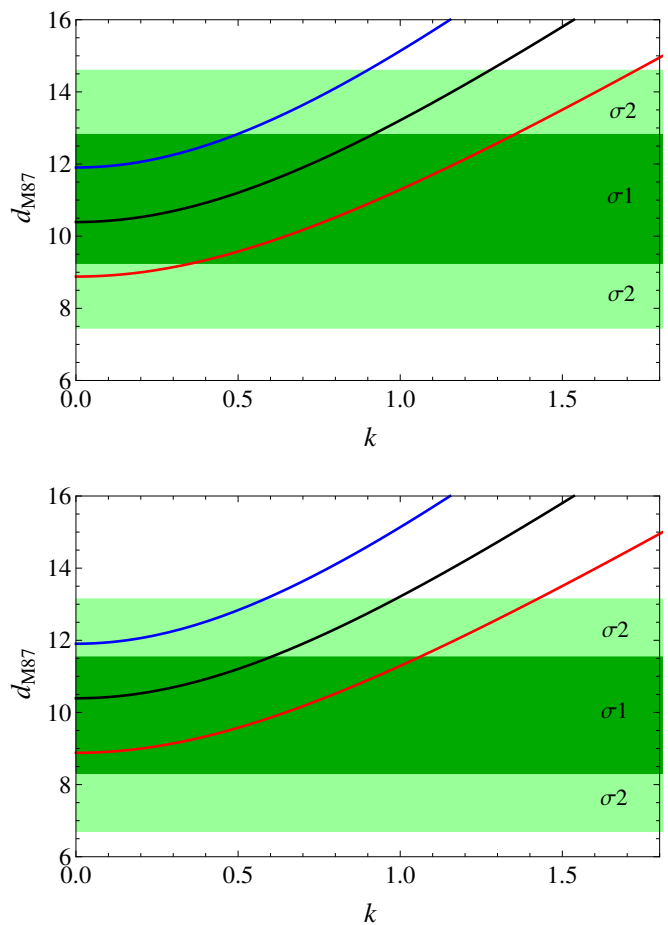


FIG. 18. Shadow diameter d_{M87} varying with k (black line) with the 1σ uncertainties shown as red and blue lines. The green and light green shaded regions, respectively, give the 1σ and 2σ confidence region for observed emission ring diameter (Top figure) and shadow angular diameter with 10% offset of M87* shadow (Bottom figure).

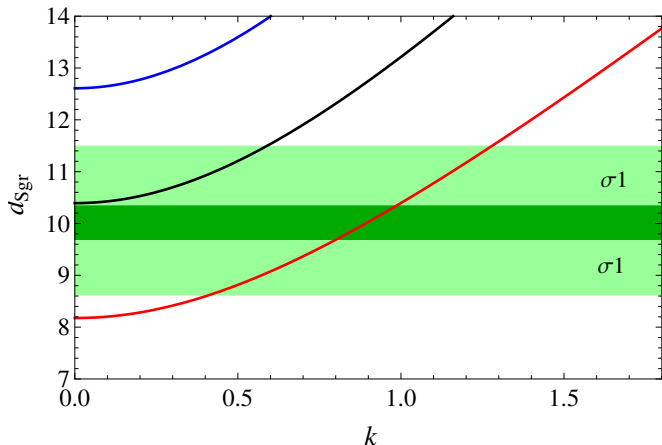


FIG. 19. Shadow diameter d_{Sgr} varying with k (black line) with the 1σ uncertainties shown as red and blue lines. The green and light green shaded regions, respectively, give the average value and a 1σ confidence region for the observed Sgr A* shadow angular diameter.

Interferometer (VLTI) observations and the three independent imaging models to estimate the bounds on the fraction deviation observable δ [21, 22]

$$\delta = \begin{cases} -0.08^{+0.09}_{-0.09} & \text{VLTI} \\ -0.04^{+0.09}_{-0.10} & \text{Keck} \end{cases} \quad (104)$$

Figure 19 depicts the shadow diameter for the polymerized black hole model of the Sgr A* black hole. The average value and the 1σ bound of shadow diameter place a constraint on the upper value of the k (cf. fig. 19). With $M = 4.0 \times 10^6 M_\odot$ and $DLS = 8.15$ kpc, polymerized black hole with $k \leq 0.588$ satisfies the 1σ bound for Sgr A* shadow size (black line in Fig. 19). However, given the mass and distance uncertainties of the Sgr A* black hole, the polymerized black hole shadow with $k \leq 1.281$ is consistent with the Sgr A* shadow within 1σ (red line in Fig. 19). In Fig. 20, we depict the δ , measuring the fractional deviation of the polymerized black hole shadow diameter from that of a Schwarzschild black hole. Following [21], we choose the `ehtimaging +Keck+GRMHD` and `eht-imaging +VLTI+GRMHD` combinations as the two fiducial cases to calculate constraints on the polymerized black hole parameter. In particular, Keck and VLTI measurements within the 1σ confidence interval, respectively, constraint $k \leq 0.396$ and $k \leq 0.180$.

VIII. CONCLUSION

In this paper, we have carried out a comprehensive study of the static and spherically symmetric polymerized black holes. These black holes are motivated by the LQG principles and semi-polymerization

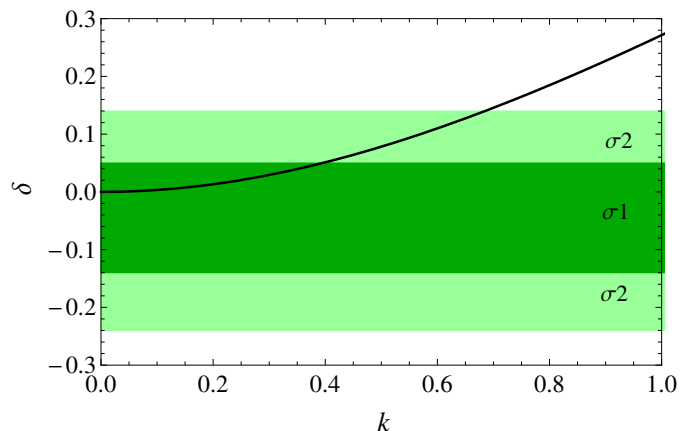
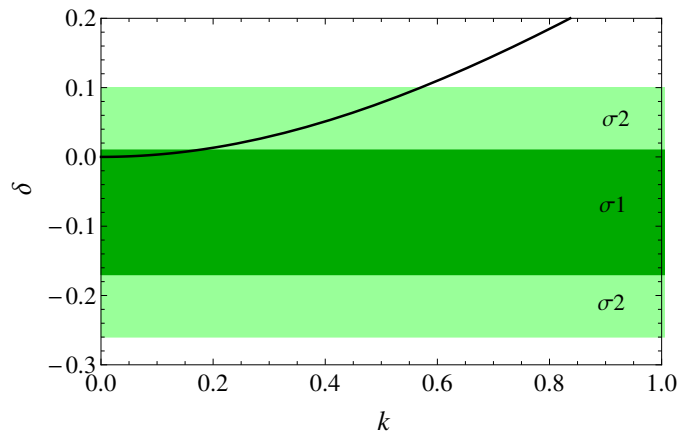


FIG. 20. Fractional diameter deviation observable δ varying with k . The green and light green shaded regions, respectively, give the 1σ and 2σ confidence regions for the observed Sgr A* shadow deviation from that of a Schwarzschild black hole with the VLTI estimate (*Top figure*) and Keck estimate (*Bottom figure*).

technique. In addition, these black holes are not only free from the curvature singularity at the center and are globally regular, but also free from the blue-shift mass instability at the inner horizon as they possess only a single horizon. This salient feature makes them distinct from the other class of regular black holes. We began by showing that the polymerized black hole metric arises naturally as a solution of Einstein field equations sourced by the phantom scalar field and magnetic field associated with the NED field. Then we addressed the question of whether the quantum corrections around the $r = 0$ can leave imprints at observationally accessible length scales. To answer this, we computed the light deflection angle in the weak and strong gravitational lensing limits, and calculated the image position magnification and time delay. We compared the obtained results for the polymerized black hole with those corresponding to the Schwarzschild black hole. Using the ray-tracing technique, we identified the range of light impact

parameter contributing to the direct, lensed, and photon ring emission. Black hole shadows under different accretion models are constructed.

The following are the major outcomes

- In the limit $k \rightarrow 0$, the polymerized black hole metric recover the Schwarzschild metric, and the horizon size increases with k .
- Contrary to Schwarzschild black holes, the polymerized black holes possess both the unstable and stable photon circular orbits. The unstable (stable) orbits are outside (inside) the event horizon.
- In the polymerized black hole spacetime, although the images form farther away from the black hole center, they are more magnified compared to the Schwarzschild black hole.
- The observed peak luminosity decreases with the increases of k .
- Polymerized black holes have larger shadows with darker interior than those for the Schwarzschild black hole.
- The shadow contrast is significantly large for the radially infalling accreting gas compared to that for static gas for the same value of k .
- The observed maximum luminosity is lower for the infalling accretion than that of the static model for the same value of k .
- Polymerized black holes have thicker lensing and photon rings compared to those for the Schwarzschild black hole.

- For the thin disk accretion, there is not only a dark central area, but also the photon rings and lensing rings outside of black hole shadow.
- Polymerized black holes with $k \leq 0.588$ satisfy the 1σ bound for the observed Sgr A* shadow angular diameter.
- Polymerized black holes with $k \leq 0.60$ satisfy the 1σ bound for the observed M87* shadow angular diameter.
- Keck and VLTI measurements of δ for the Sgr A* black hole shadow put constraints, receptively, $k \leq 0.396$ and $k \leq 0.180$.

In this work, we restricted ourselves only to non-rotating spacetime. Interesting features can be anticipated by the inclusion of the rotation. The gravitational lensing and shadow of the rotating polymerized black holes are part of future work. However, given the significance of accretion upon black holes, a proper understanding necessitates relativistic magnetohydrodynamic simulations of the hot plasma flow with effects of magnetic fields. These are beyond the scope of the present paper. In summary, we have shown that the quantum gravity effects, coming from the polymerization, are accessible in the astrophysical black holes' observations.

IX. ACKNOWLEDGMENTS

R.K.W. would like to thank Prof. Sunil Maharaj and the University of KwaZulu-Natal for their support. R.K.W. also thanks Prof. Kirill Bronnikov and Dr. Rajibul Shaik for the fruitful discussions. R.K.W. thanks Prof. Sunil Maharaj and Prof. Sushant Ghosh for the comments on the initial draft.

-
- [1] J. R. Oppenheimer and H. Snyder, Phys. Rev. **56**, 455 (1939).
 - [2] R. Penrose, Riv. Nuovo Cim. **1**, 252 (1969) [Gen. Rel. Grav. **34**, 1141 (2002)].
 - [3] C. Rovelli and L. Smolin, Nucl. Phys. B **442**, 593 (1995) [erratum: Nucl. Phys. B **456**, 753 (1995)].
 - [4] C. Rovelli, Living Rev. Rel. **1**, 1 (1998).
 - [5] L. Modesto, Phys. Rev. D **70**, 124009 (2004).
 - [6] L. Modesto, Class. Quant. Grav. **23**, 5587 (2006).
 - [7] A. Ashtekar and M. Bojowald, Class. Quant. Grav. **23**, 391 (2006).
 - [8] A. Ashtekar, S. Fairhurst and J. L. Willis, Class. Quant. Grav. **20**, 1031 (2003).
 - [9] C. G. Boehmer and K. Vandersloot, Phys. Rev. D **76**, 104030 (2007).
 - [10] A. Peltola and G. Kunstatter, Phys. Rev. D **79**, 061501 (2009).
 - [11] A. Peltola and G. Kunstatter, Phys. Rev. D **80**, 044031 (2009).
 - [12] R. G. Daghigh, M. D. Green, J. C. Morey and G. Kunstatter, Phys. Rev. D **102**, 104040 (2020).
 - [13] R. Carballo-Rubio, F. Di Filippo, S. Liberati, C. Pacilio and M. Visser, JHEP **07**, 023 (2018).
 - [14] K. A. Bronnikov, V. N. Melnikov and H. Dehnen, Gen. Rel. Grav. **39**, 973 (2007).
 - [15] V. Bozza, S. Capozziello, G. Iovane and G. Scarpetta, Gen. Rel. Grav. **33**, 1535 (2001).
 - [16] V. Bozza, Phys. Rev. D **66**, 103001 (2002).
 - [17] J. M. Bardeen, *Black Holes*, Edited by C. DeWitt and B. S. DeWitt (Gordon and Breach, New York, 1973, p. 215).
 - [18] K. Akiyama *et al.*, Astrophys. J. **875**, L1 (2019).
 - [19] K. Akiyama *et al.*, Astrophys. J. **875**, L5 (2019).
 - [20] K. Akiyama *et al.*, Astrophys. J. **875**, L6 (2019).

- [21] K. Akiyama *et al.*, *Astrophys. J. Lett.* **930**, L12 (2022).
- [22] K. Akiyama *et al.*, *Astrophys. J. Lett.* **930**, L16 (2022).
- [23] K. Akiyama *et al.*, *Astrophys. J. Lett.* **930**, L14 (2022).
- [24] K. Akiyama *et al.*, *Astrophys. J. Lett.* **930**, L17 (2022).
- [25] C. Liu, T. Zhu, Q. Wu, K. Jusufi, M. Jamil, M. Azreg-Aïnou and A. Wang, *Phys. Rev. D* **101**, 084001 (2020).
- [26] T. Zhu and A. Wang, *Phys. Rev. D* **102**, 124042 (2020).
- [27] S. Brahma, C. Y. Chen and D. h. Yeom, *Phys. Rev. Lett.* **126**, 181301 (2021).
- [28] Q. M. Fu and X. Zhang, *Phys. Rev. D* **105**, 064020 (2022).
- [29] S. W. Wei, P. Cheng, Y. Zhong and X. N. Zhou, *JCAP* **08**, 004 (2015).
- [30] X. X. Zeng, G. P. Li and K. J. He, *Nucl. Phys. B* **974**, 115639 (2022).
- [31] A. Held, R. Gold and A. Eichhorn, *JCAP* **06**, 029 (2019).
- [32] R. Kumar, B. P. Singh and S. G. Ghosh, *Annals Phys.* **420**, 168252 (2020).
- [33] A. Einstein, *Science* **84**, 506 (1936).
- [34] C. Darwin, *Proc. R. Soc. A* **249**, 180 (1959).
- [35] J. L. Synge, *Mon. Not. R. Astron. Soc.* **131**, 463 (1966).
- [36] S. Liebes, *Phys. Rev.* **133**, B835 (1964).
- [37] S. Refsdal, *Mon. Not. Roy. Astron. Soc.* **128**, 295 (1964).
- [38] P. Schneider, J. Ehlers, and E. E. Falco, *Gravitational Lenses* (Springer-Verlag, Berlin (1992)).
- [39] S. Frittelli, T. P. Kling and E. T. Newman, *Phys. Rev. D* **61**, 064021 (2000).
- [40] S. E. Gralla and A. Lupsasca, *Phys. Rev. D* **101**, 044031 (2020).
- [41] K. S. Virbhadra and G. F. R. Ellis, *Phys. Rev. D* **62**, 084003 (2000).
- [42] K. S. Virbhadra and G. F. R. Ellis, *Phys. Rev. D* **65**, 103004 (2002).
- [43] K. S. Virbhadra and C. R. Keeton, *Phys. Rev. D* **77**, 124014 (2008).
- [44] V. Bozza and L. Mancini, *Astrophys. J.* **611**, 1045 (2004).
- [45] V. Bozza and G. Scarpetta, *Phys. Rev. D* **76**, 083008 (2007).
- [46] V. Bozza, *Phys. Rev. D* **78**, 103005 (2008).
- [47] N. Tsukamoto, *Phys. Rev. D* **95**, 064035 (2017).
- [48] N. Tsukamoto and Y. Gong, *Phys. Rev. D* **95**, 064034 (2017).
- [49] N. Tsukamoto, *Phys. Rev. D* **102**, 104029 (2020).
- [50] N. Tsukamoto, *Phys. Rev. D* **104**, 124016 (2021).
- [51] C. T. Cunningham, J. M. Bardeen, *Astrophys. J.* **173**, L137 (1972).
- [52] J. P. Luminet, *Astron. Astrophys.* **75**, 228 (1979).
- [53] R. Narayan, M. D. Johnson and C. F. Gammie, *Astrophys. J. Lett.* **885**, L33 (2019).
- [54] V. Perlick and O. Y. Tsupko, *Phys. Rept.* **947**, 1 (2022).
- [55] P. V. P. Cunha and C. A. R. Herdeiro, *Gen. Rel. Grav.* **50**, 42 (2018).
- [56] A. Bhadra, *Phys. Rev. D* **67**, 103009 (2003).
- [57] E. F. Eiroa, *Phys. Rev. D* **71**, 083010 (2005).
- [58] C. R. Keeton and A. O. Petters, *Phys. Rev. D* **72**, 104006 (2005).
- [59] S. b. Chen and J. l. Jing, *Phys. Rev. D* **80**, 024036 (2009).
- [60] R. Reyes, R. Mandelbaum, U. Seljak, T. Baldauf, J. E. Gunn, L. Lombriser and R. E. Smith, *Nature* **464**, 256 (2010).
- [61] W. Javed, R. Babar and A. Övgün, *Phys. Rev. D* **99**, 084012 (2019).
- [62] R. Shaikh, P. Banerjee, S. Paul and T. Sarkar, *Phys. Rev. D* **99**, 104040 (2019).
- [63] H. M. Reji and M. Patil, *Phys. Rev. D* **101**, 064051 (2020).
- [64] S. U. Islam, R. Kumar and S. G. Ghosh, *JCAP* **09**, 030 (2020).
- [65] R. Kumar, S. U. Islam and S. G. Ghosh, *Eur. Phys. J. C* **80**, 1128 (2020).
- [66] K. S. Virbhadra, [arXiv:2204.01879 [gr-qc]].
- [67] K. S. Virbhadra, [arXiv:2204.01792 [gr-qc]].
- [68] H. Falcke, F. Melia and E. Agol, *Astrophys. J.* **528**, L13 (2000).
- [69] S. Doeleman *et al.*, *Nature* **455**, 78 (2008).
- [70] R. Takahashi, *J. Korean Phys. Soc.* **45**, S1808 (2004) [*Astrophys. J.* **611**, 996 (2004)].
- [71] L. Huang, M. Cai, Z. Q. Shen and F. Yuan, *Mon. Not. Roy. Astron. Soc.* **379**, 833 (2007).
- [72] K. Hioki and K. i. Maeda, *Phys. Rev. D* **80**, 024042 (2009).
- [73] D. Psaltis, F. Ozel, C. K. Chan and D. P. Marrone, *Astrophys. J.* **814**, 115 (2015).
- [74] A. A. Abdujabbarov, L. Rezzolla, and B. J. Ahmedov, *Mon. Not. R. Astron. Soc.* **454**, 2423 (2015).
- [75] Y. Mizuno *et al.*, *Nat. Astron.* **2**, 585 (2018).
- [76] R. Shaikh, *Phys. Rev. D* **100**, 024028 (2019).
- [77] A. K. Mishra, S. Chakraborty and S. Sarkar, *Phys. Rev. D* **99**, 104080 (2019).
- [78] R. A. Konoplya and A. Zhidenko, *Phys. Rev. D* **100**, 044015 (2019).
- [79] S. E. Gralla, *Phys. Rev. D* **102**, 044017 (2020).
- [80] R. Kumar, S. G. Ghosh and A. Wang, *Phys. Rev. D* **100**, 124024 (2019).
- [81] R. Kumar and S. G. Ghosh, *JCAP* **07**, 053 (2020).
- [82] R. Kumar, S. G. Ghosh and A. Wang, *Phys. Rev. D* **101**, 104001 (2020).
- [83] R. Roy, S. Vagnozzi and L. Visinelli, *Phys. Rev. D* **105**, 083002 (2022).
- [84] R. Roy and U. A. Yajnik, *Phys. Lett. B* **803**, 135284 (2020).
- [85] R. Shaikh, P. Kocherlakota, R. Narayan and P. S. Joshi, *Mon. Not. Roy. Astron. Soc.* **482**, 52-64 (2019).
- [86] T. Bronzwaer and H. Falcke, *Astrophys. J.* **920**, 155 (2021).
- [87] M. Afrin, R. Kumar and S. G. Ghosh, *Mon. Not. Roy. Astron. Soc.* **504**, 5927 (2021).
- [88] S. G. Ghosh, R. Kumar and S. U. Islam, *JCAP* **03**, 056 (2021).
- [89] R. Kumar, A. Kumar and S. G. Ghosh, *Astrophys. J.* **896**, 89 (2020).
- [90] R. Kumar and S. G. Ghosh, *Class. Quant. Grav.* **38**, 8 (2021).
- [91] R. Kumar and S. G. Ghosh, *Astrophys. J.* **892**, 78 (2020).
- [92] S. Nampalliwar and S. K, [arXiv:2108.01190 [gr-qc]].
- [93] S. Nampalliwar, S. Kumar, K. Jusufi, Q. Wu, M. Jamil and P. Salucci, *Astrophys. J.* **916**, 116 (2021).
- [94] S. Devi, A. N. S, S. Chakrabarti and B. R. Majhi, [arXiv:2105.11847 [gr-qc]].
- [95] S. E. Gralla, A. Lupsasca and D. P. Marrone, *Phys. Rev. D* **102**, 124004 (2020).
- [96] K. A. Bronnikov and J. C. Fabris, *Phys. Rev. Lett.* **96**, 251101 (20)

- [97] K. A. Bronnikov and P. A. Korolyov, *Grav. Cosmol.* **21**, 157 (2015).
- [98] K. A. Bronnikov, *Particles* **1**, 56 (2018).
- [99] A. Ashtekar and J. Lewandowski, *Class. Quant. Grav.* **21**, R53 (2004).
- [100] K. A. Bronnikov and R. K. Walia, *Phys. Rev. D* **105**, 044039 (2022).
- [101] K. A. Bronnikov, *Phys. Rev. D* **63**, 044005 (2001).
- [102] S. Weinberg, *Gravitation and Cosmology: Principles and Applications of the General Theory of Relativity* (New York: Wiley, 1972).
- [103] S. Chandrasekhar, *The Mathematical Theory of Black Holes* (Oxford University Press, New York, 1992).
- [104] E. F. Eiroa, [arXiv:1212.4535 [gr-qc]].
- [105] K. S. Virbhadra, *Phys. Rev. D* **79**, 083004 (2009).
- [106] T. Do *et al.*, *Science* **365**, 664 (2019).
- [107] Y. Zhu, R. Narayan, A. Sadowski and D. Psaltis, *Mon. Not. Roy. Astron. Soc.* **451**, 1661 (2015)
- [108] R. Narayan, Y. Zhu, D. Psaltis and A. Sadowski, *Mon. Not. Roy. Astron. Soc.* **457**, 608 (2016).
- [109] A. Chael, M. D. Johnson and A. Lupsasca, *Astrophys. J.* **918**, 6 (2021).
- [110] S. E. Gralla, D. E. Holz and R. M. Wald, *Phys. Rev. D* **100**, 024018 (2019).
- [111] A. E. Broderick, P. Tiede, D. W. Pesce and R. Gold, *Astrophys. J.* **927**, 6 (2022)
- [112] K. Beckwith and C. Done, *Mon. Not. Roy. Astron. Soc.* **359**, 1217-1228 (2005).
- [113] M. Jaroszynski and A. Kurpiewski, *Astron. Astrophys.* **326**, 419 (1997).
- [114] C. Bambi, *Phys. Rev. D* **87**, 107501 (2013).
- [115] S. Guo, G. R. Li and E. W. Liang, *Phys. Rev. D* **105**, 023024 (2022).
- [116] M. Guerrero, G. J. Olmo, D. Rubiera-Garcia and D. S. C. Gómez, *JCAP* **08**, 036 (2021).
- [117] A. Uniyal, R. C. Pantig and A. Övgün, [arXiv:2205.11072 [gr-qc]].
- [118] G. P. Li and K. J. He, *JCAP* **06**, 037 (2021).
- [119] M. Okyay and A. Övgün, *JCAP* **01**, 009 (2022).
- [120] G. S. Bisnovatyi-Kogan and O. Y. Tsupko, *Phys. Rev. D* **105**, 064040 (2022).
- [121] M. Wielgus, *Phys. Rev. D* **104**, 124058 (2021).
- [122] R. Shaikh and P. S. Joshi, *JCAP* **10**, 064 (2019).
- [123] A. B. Joshi, D. Dey, P. S. Joshi and P. Bambhaniya, *Phys. Rev. D* **102**, 024022 (2020).
- [124] P. Kocherlakota *et al.* [Event Horizon Telescope], *Phys. Rev. D* **103**, 104047 (2021).
- [125] S. Vagnozzi, R. Roy, Y. D. Tsai and L. Visinelli, [arXiv:2205.07787 [gr-qc]].
- [126] S. G. Ghosh and M. Afrin, [arXiv:2206.02488 [gr-qc]].
- [127] S. Vagnozzi and L. Visinelli, *Phys. Rev. D* **100**, 024020 (2019).
- [128] C. Bambi, K. Freese, S. Vagnozzi and L. Visinelli, *Phys. Rev. D* **100**, 044057 (2019).
- [129] A. Allahyari, M. Khodadi, S. Vagnozzi and D. F. Mota, *JCAP* **02**, 003 (2020).
- [130] D. Psaltis *et al.* [Event Horizon Telescope], *Phys. Rev. Lett.* **125**, 141104 (2020).
- [131] Z. Younsi, D. Psaltis and F. Özel, [arXiv:2111.01752 [astro-ph.HE]].
- [132] M. Afrin and S. G. Ghosh, *Astrophys. J.* **932**, 51 (2022).
- [133] S. E. Gralla, *Phys. Rev. D* **103**, 024023 (2021).